Nucleic Acids Research, 2023, **51**, 11142–11161
https://doi.org/10.1093/nar/gkad798
Advance access publication date: 9 October 2023
Genomics

Lineage specific 3D genome structure in the adult human brain and neurodevelopmental changes in the chromatin interactome

Samir Rahman[1,2,3,4,5,*,†], Pengfei Dong[1,2,3,4,5,†], Pasha Apontes[1,2,3,4,5,6,†], Michael B. Fernando[2,7,8], Roman Kosoy[1,2,3,4,5], Kayla G. Townsley[2,7], Kiran Girdhar[1,2,3,4,5], Jaroslav Bendl[1,2,3,4,5], Zhiping Shao[1,2,3,4,5], Ruth Misir[1,2,3,4,5], Nadia Tsankova[7,9], Steven P. Kleopoulos[1,2,3,4,5], Kristen J. Brennand[2,4,7,8,10], John F. Fullard[1,2,3,4,5] and Panos Roussos[1,2,3,4,5,6,11,*]

[1]Center for Disease Neurogenomics, Icahn School of Medicine at Mount Sinai, New York, NY 10029, USA
[2]Friedman Brain Institute, Icahn School of Medicine at Mount Sinai, New York, NY 10029, USA
[3]Icahn Institute for Data Science and Genomic Technology, Icahn School of Medicine at Mount Sinai, New York, NY 10029, USA
[4]Department of Psychiatry, Icahn School of Medicine at Mount Sinai, New York, NY 10029, USA
[5]Department of Genetics and Genomic Sciences, Icahn School of Medicine at Mount Sinai, New York, NY 10029, USA
[6]Mental Illness Research Education and Clinical Center (MIRECC), James J. Peters VA Medical Center, Bronx, NY 10468, USA
[7]Department of Neuroscience, Icahn School of Medicine at Mount Sinai, New York, NY 10029, USA
[8]Black Family Stem Cell Institute, Icahn School of Medicine at Mount Sinai, New York, NY 10029, USA
[9]Department of Pathology, Molecular, and Cell-based Medicine, Icahn School of Medicine at Mount Sinai, New York, NY 10029, USA
[10]Current address: Department of Psychiatry, Yale University, New Haven, CT 06511, USA
[11]Center for Dementia Research, Nathan Kline Institute for Psychiatric Research, Orangeburg, NY 10962, USA

[*]To whom correspondence should be addressed. Tel: +1 212 824 8982; Email: panagiotis.roussos@mssm.edu
Correspondence may also be addressed to Samir Rahman. Tel: +1 347 554 1857; Email: Samir.rahman@mssm.edu
[†]The authors wish it to be known that, in their opinion, the first three authors should be regarded as Joint First Authors.

Abstract

The human brain is a complex organ comprised of distinct cell types, and the contribution of the 3D genome to lineage specific gene expression remains poorly understood. To decipher cell type specific genome architecture, and characterize fine scale changes in the chromatin interactome across neural development, we compared the 3D genome of the human fetal cortical plate to that of neurons and glia isolated from the adult prefrontal cortex. We found that neurons have weaker genome compartmentalization compared to glia, but stronger TADs, which emerge during fetal development. Furthermore, relative to glia, the neuronal genome shifts more strongly towards repressive compartments. Neurons have differential TAD boundaries that are proximal to active promoters involved in neurodevelopmental processes. CRISPRi on *CNTNAP2* in hIPSC-derived neurons reveals that transcriptional inactivation correlates with loss of insulation at the differential boundary. Finally, re-wiring of chromatin loops during neural development is associated with transcriptional and functional changes. Importantly, differential loops in the fetal cortex are associated with autism GWAS loci, suggesting a neuropsychiatric disease mechanism affecting the chromatin interactome. Furthermore, neural development involves gaining enhancer-promoter loops that upregulate genes that control synaptic activity. Altogether, our study provides multi-scale insights on the 3D genome in the human brain.

Received: March 3, 2023. **Revised:** August 18, 2023. **Editorial Decision:** September 17, 2023. **Accepted:** September 19, 2023

Graphical abstract

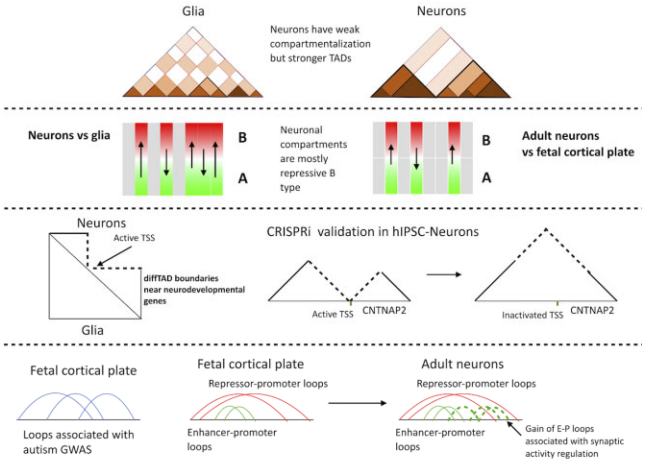

Introduction

The spatiotemporal organization of the genome plays a key role in the regulation of gene expression, the disruption of which has been linked to disease (1–3). Chromosomes are partitioned into megabase-sized compartments, named A and B, which contain active and repressed chromatin, respectively (4). Compartments are further separated into self-interacting neighborhoods called topologically associated domains (TADs) that are segregated from each other by CTCF bound insulator elements, the disruption of which promotes aberrant enhancer-promoter interactions and transcription mis-regulation (5–7).

The 3D structure of chromatin changes during neural development (8). Studies of mouse and human embryonic stem cells have shown that neural differentiation leads to compartment switching and changes in intra- and inter-TAD interactions (9,10). Moreover, mouse neural differentiation is also associated with the formation of enhancer-promoter loops and *de novo* TADs correlated with neural gene activation (11). Chromatin interactome studies in human iPSC derived neurons and fetal brain revealed the importance of distal enhancers in regulating genes implicated in neuronal function. These regulatory sequences were also shown to be enriched for genetic variants of schizophrenia (SCZ), a psychiatric disorder characterized by abnormal neuronal connectivity (12–14). In addition to SCZ, the chromatin interactome has been used to investigate the causal mechanisms of a range of brain diseases, including bipolar disorder (BD) and Alzheimer's disease (AD) (15).

Although promoter-centric interactions have been identified in different cell types in fetal and adult human brain (16,17), a comprehensive study of the different scales of chromatin organization, from compartments to loops and their roles in regulating gene expression is lacking. Furthermore, previous studies have not investigated the re-wiring of the chromatin interactome across human brain development. To address these gaps in our knowledge, we applied a multi-omics approach (integrating deeply sequenced Hi-C with ChIP-seq and RNA-seq) to specimens of fetal cortical plate and adult prefrontal cortex. The resulting data allowed us to examine the fine scale remodeling of chromatin interactions that occurs during neural development, as well as differences in 3D chromatin structure between various cell types in the adult brain.

Materials and methods

Description of post-mortem brain samples

Fetal brain samples were collected from de-identified prenatal autopsy specimens without neuropathological abnormalities at the Icahn School of Medicine at Mount Sinai. The cortical plate was dissected fresh from the anterior frontal lobe of anatomically intact brain specimens. Young and old adult brain samples were accessed through the NIH NeuroBioBank at the Mount Sinai Brain Bank and the University of Miami Brain Endowment Bank. All neuropsychological, diagnostic and autopsy protocols were approved by the respective Institutional Review Boards.

Isolation of nuclei from frozen human brain specimens

50 mg of frozen brain tissue was homogenized in chilled lysis buffer (0.32 M Sucrose, 5 mM $CaCl_2$, 3 mM magnesium acetate, 0.1 mM, EDTA, 10 mM Tris–HCl, pH 8, 1 mM DTT, 0.1% Triton X-100) and filtered through a 40 μm cell strainer. Filtered lysate was then underlaid with sucrose solution (1.8 M Sucrose, 3 mM $Mg(CH_3COO)_2$, 1 mM DTT, 10 mM Tris–HCl, pH 8) and subjected to ultracentrifugation at 107 000 × g for 1 h at 4°C. Pellets were resuspended in 500 μl DPBS containing 0.1% BSA. For non-fetal tissue, anti-NeuN antibody (1:1000, Alexa488 conjugated, Millipore, Cat# MAB377X) was added and samples incubated, in the dark, for 1 h at 4°C. Prior to FANS sorting, DAPI (Thermoscientific) was added to a final concentration of 1 μg/ml. DAPI positive neuronal (NeuN+) and non-neuronal/glial (NeuN-) nuclei were isolated using a FACSAria flow cytometer with FACSDiva Version 8.0.1 software (BD Biosciences). In the case of fetal tissue, where NeuN is not expressed, nuclei were isolated using DAPI staining only.

in situ Hi-C on frozen human brain tissue

Hi-C data was generated from frozen postmortem human brain tissue using the *in situ* Hi-C protocol (18) with some

modifications. Briefly, frozen prefrontal cortex tissue was thawed at room temperature (RT) and dounce homogenized in HBSS (Hank's balanced salt solution). Homogenized tissue was fixed with 0.5% formaldehyde for 10 min and then quenched with 0.125 M glycine for 5 min at RT. Cross-linked tissue was then placed on ice for a further 15 min to quench crosslinking completely. Tissue was pelleted at 800 × g for 10 min at 4°C and then resuspended in lysis buffer (0.32 M sucrose, 5 mM $CaCl_2$, 3 mM $Mg(CH_3COO)_2$, 0.1 mM EDTA, 10 mM Tris–HCl, pH 8, 1 mM DTT, 0.1% Triton X-100, 1 Roche cOmplete mini EDTA-free protease inhibitor tablet, Roche Cat# 4693159001) to isolate cross-linked nuclei.

Approximately 1 M crosslinked nuclei from fetal cortical plate, or neuronal and non-neuronal (glia) nuclei from adult brains, were thawed on ice, washed with ice cold 1x CutSmart buffer (New England Biolabs (NEB), Cat# B7204S) and split into four aliquots to generate technical replicate libraries per sample, with 250k nuclei per library. Nuclei were pelleted at 2500 × g for 5 min at 4°C, and resuspended in 342 μl 1× CutSmart buffer and then conditioned with 0.1% SDS at 65°C for 10 min. Nuclei were immediately placed on ice and the SDS quenched with 1% Triton X-100. Chromatin was digested with 100 U of the 4 bp cutter MboI (New England Biolabs, Cat# R0147L) overnight at 37°C with shaking at 400 rpm. MboI was heat inactivated at 65°C for 20 min, and then nuclei were cooled down on ice. MboI cut sites were end labeled with biotin by adding 52 μl of biotin fill-in reaction mix (15 μl of 1 mM biotin-14-dATP (Jena Bioscience, Cat# NU-835-BIO14-L), 1.5 μl each of 10 mM dCTP, dGTP, dTTP (Sigma-Aldrich, Cat# DNTP10-1KT), 10 μl of 5 U/μl Klenow DNA Pol I (New England Biolabs, Cat# M0210L), 22.5 μl of 1× CutSmart buffer) and shaking at 37°C for 1.5 h at 400 rpm. Blunt ended sites were proximity ligated by adding 948 μl ligation reaction mix (150 μl of 10× T4 DNA ligase buffer (New England Biolabs, Cat# B0202S), 125 μl of 10% Triton X-100, 15 μl of 10 mg/ml BSA, 10 μl of 400 U/μl T4 DNA ligase (New England Biolabs, Cat# M0202L), 648 μl ddH_20) and rotating tubes, end-over-end, at RT for 4 h. Nuclei were reverse crosslinked with 100 μl proteinase K (10 mg/ml) overnight at 65°C.

Proximity ligated DNA was purified through phenol:chloroform extraction and sodium acetate/ethanol precipitation. Purified DNA was sheared using a Covaris S220 sonicator to generate a peak size of 400 bp with the following settings (peak incident power: 140 W, duty cycle: 10%, cycles per burst: 200, time: 55 sec). Biotin labeled ligation junctions were purified with Dynabeads MyOne Streptavidin C1 beads (ThermoFisher, Cat# 65001) by incubating for 1 hr at RT. Illumina compatible libraries were prepared from the sonicated and streptavidin bead immobilized DNA using the NEBNext Ultra II Library prep kit (New England Biolabs, Cat# E7645L), following manufacturer's instructions, amplifying libraries for 6–13 PCR cycles. Libraries were purified by two-sided size selection (300–800 bp) using Ampure XP beads (Beckman Coulter, Cat# A63881). All libraries were analyzed on a TapeStation using Agilent D5000 ScreenTapes, and quantified using the KAPA Library Quantification Kit (Roche, Cat# KK4873) prior to sequencing. Uniquely barcoded Hi-C libraries were pooled and deep sequenced on the Illumina NovaSeq S4 platform obtaining 100 bp paired end reads, to generate approximately 250 million reads per library.

Native ChIP-seq

Ultra-low input Native Chromatin Immunoprecipitation sequencing (ULI-NChIP-seq) libraries were prepared as follows. After FANs-sorting of neuronal (NeuN+) and non-neuronal nuclei (NeuN- nuclei), we performed ULI-NChIP assays, adapted from (19), which specifically does not require chromatin crosslinking, thereby increasing library complexity and reducing PCR artifacts. Briefly, nuclei were centrifuged at 500 × g for 10 min at 4°C and re-suspended by gentle pipetting in residual smaller volumes of PBS/Sheath buffer. After DAPI counting of nuclei, 100–300K were distributed into Eppendorf tubes and 0.1% Triton-X-100/0.1% Na-Deoxycholate added. The chromatin was re-suspended and placed at room temperature for 5 min, followed by fragmentation with micrococcal nuclease (MNase, NEB, Cat#M0247S) for 5 min at 37°C on a ThermoMixer at 800 rpm to digest the chromatin to predominantly mononucleosomes. The MNase reaction was stopped by addition of 10% of the reaction volume of 100 mM EDTA (pipetted ∼20x), followed by the addition of 1% Triton/1% deoxycholate, (pipetted 5x) and placed on ice for at least 15 min. Samples were vortexed (medium setting) for ∼ 30 s and complete NChIP buffer (20 mM Tris–HCl, pH 8.0, 2 mM EDTA, 15 mM NaCl, 0.1% Triton X-100, 1 EDTA-free protease inhibitor cocktail and 1 mM phenylmethanesulfonyl fluoride) was added to dilute the chromatin to <25% of the immunoprecipitation reaction volume, and rotated at 4°C for 1 h. After the incubation, chromatin was vortexed (medium setting) for ∼30 s and 5% input controls removed for DNA extraction.

To avoid non-specific binding, chromatin was next precleared by adding 10 μl/ reaction of a pre-washed 1:1 ratio of protein A to protein G Dynabeads (ThermoFisher, Cat# 10001D and #10003D), rotating the chromatin-protein A/protein G magnetic bead mixture for 3 h at 4°C. Antibody-bead complexes were prepared as follows: ChIP-grade histone antibodies H3K27ac (Active Motif, Cat# 39133, pAB), H3K4me3 (Cell Signaling, Cat# 9751), or H3K27me3 (Cell Signaling, Cat# 9733) were added to prewashed protein A/protein G Dynabeads resuspended in NChIP buffer, and the antibody-bead complexes formed by rotating the antibody and beads for 2 h at 4°C. After the incubations, precleared chromatin and antibody-bead complexes were placed on a magnetic rack and the precleared chromatin transferred to new Eppendorf tubes, while the antibody-bead complexes were resuspended in sufficient volume of NChIP buffer to add 10 μl per MNase reaction. The chromatin was immunoprecipitated with the antibody-bead complexes at 4°C overnight while rotating.

After the overnight incubation, the immunoprecipitation reactions were placed on a magnetic rack to remove unbound chromatin, washed twice with 200 μl of ChIP low salt wash buffer (20 mM Tris–HCl, pH 8.0, 0.1% SDS, 1% Triton X-100, 0.1% deoxycholate, 2 mM EDTA and 150 mM NaCl), twice with 200 μl ChIP high salt wash buffer (20 mM Tris–HCl (pH 8.0), 0.1% SDS, 1% Triton X-100, 0.1% deoxycholate, 2 mM EDTA and 500 mM NaCl), followed by elution in freshly prepared 30 μl of ChIP elution (100 mM sodium bicarbonate and 1% SDS) for 1.5 h at 68°C on a ThermoMixer at 1000 rpm, RNAse A digestion for 15 min at 37°C at 800 rpm. The immunoprecipitated DNA, along with the input controls, was purified using Phenol:Chloroform:Isoamyl Alcohol (25:24:1, v/v) (ThermoFisher Scientific, Cat# 15593-

031), transferred to pre-spun phase lock tubes (Qiagen Maxtract, Cat# 129046) to obtain the aqueous layer. An overnight ethanol precipitation was performed by adding to the 10 μl of 3 M sodium acetate/100 μl aqueous layer of ChIP DNA, 1 μl of LPA (linear polyacrylamide, Sigma, Cat# 56575) and 1 μl Glycoblue (Invitrogen, Cat#AM9515).

NEBNext Ultra I DNA Library Prep Kit (New England Biolabs, Cat# E7370L) was used to construct Native ChIP-seq libraries according to the manufacturer's directions, followed by Pippin Size selection using 2% Agarose Gel cassettes (SAGE Science) and cleanup with 1.8 volumes of SPRIselect beads (Beckman Coulter, #B23318). All libraries were analyzed on a TapeStation using Agilent High Sensitivity D1000 ScreenTapes, and quantified using the KAPA Library Quantification Kit (Roche, Cat# KK4873) prior to sequencing. Uniquely barcoded libraries were pooled and sequenced on the Illumina NovaSeq S4 platform obtaining 100 bp paired end reads. Approximately 40 million paired-end reads were generated per sample and subsequently aligned on hg38.

RNA-seq

For RNA-seq, nuclei were sorted into 1.5 ml low-binding Eppendorf tubes containing Extraction buffer, a component of the PicoPure RNA Extraction kit (Arcturus, Cat# KIT0204). RNA was isolated in accordance with the PicoPure RNA Isolation kit's manufacturer's instructions. This included an RNase-free DNase treatment step (Qiagen, Cat # 79254), which was completed according to the instructions provided by the manufacturer. Samples were eluted in RNase-free water and stored at -80°C until preparation of RNA-sequencing libraries using the SMARTer Stranded Total RNA-seq Pico Kit v1 or v2 (Takara Clontech Laboratories, Cat# 635005 or 634414, respectively), according to the manufacturer's instructions. Resulting RNA-seq libraries were analyzed on a TapeStation (Agilent Technologies) using a High Sensitivity D1000 ScreenTape (Agilent, Cat# 5067–5584) and quantification of the libraries was performed using the KAPA Library Quantification Kit. RNA-seq libraries were subsequently sequenced on the Illumina NovaSeq S4 platform yielding 100 bp paired-end reads.

in situ Hi-C on CRISPRi validated Ngn2 induced neurons

Transduced Ngn2 neurons were grown in 12 well plates for *in situ* Hi-C. Media was removed and cells were washed once with 1x PBS, and then fixed with 2% formaldehyde/1× PBS for 10 min at RT. Formaldehyde fixation was quenched with 0.125 M glycine for 5 min at RT. Plates were then kept on ice for 15 min to quench cross-linking completely. Cells were gently scraped off the wells into 1.5 ml eppendorf tubes. Cells were pelleted at 800 × g for 5 min at 4°C and then washed twice with 1× PBS. After removing the supernatant, cells were frozen on dry ice for 20 min and then stored at –80°C.

Hi-C libraries were prepared from cells (NSB2607-1-4) that were transduced with the top scoring guide (Supplementary Table S1) for *CNTNAP2* (replicate libraries from 3 wells), which was shown by TaqMan qPCR (Supplementary Table S2) to downregulate gene expression at least 20-fold, and cells (NSB2607-1-4) that were transduced with the scrambled guide (replicate libraries from 6 wells). Libraries were prepared using the Arima-HiC + kit, following manufacturer's instructions, with the following modifications. Purified proximity ligated DNA was sheared using a Covaris S220 sonicator to generate a peak size of 400 bp with the following settings (peak incident power: 140 W, duty cycle: 10%, cycles per burst: 200, time: 55 s). Biotin labeled ligation junctions were purified with Dynabeads MyOne Streptavidin C1 beads (ThermoFisher, Cat# 65001) by incubating for 1 hr at RT. Illumina compatible libraries were prepared from the sonicated and streptavidin bead immobilized DNA using the NEBNext Ultra II Library prep kit (NEB, Cat# E7645L), following manufacturer's instructions, amplifying libraries for 6–11 PCR cycles. Libraries were purified by 2-sided size selection (300–800 bp) using Ampure XP beads (Beckman Coulter, Cat# A63881). All libraries were analyzed on a TapeStation using Agilent D5000 ScreenTapes, and quantified using the KAPA Library Quantification Kit prior to sequencing. Uniquely barcoded Hi-C libraries were pooled and deep sequenced on the Illumina NovaSeq S4 platform obtaining 100 bp paired end reads, to generate approximately 250 million reads per library. RNA-seq libraries were prepared from the same cells (Supplementary Table S3). Details about guide RNA design, plasmid preparation, lentiviral transduction and CRISPRi knockdown validation are presented in Supplementary Methods.

RNA-seq data processing

The trimmed reads were aligned to human genome hg38 (GRCh38) using STAR (2.7.2a) aligner (20), where the allelic alignment bias was corrected by WASP (21). Gene expression was quantified using RSEM (v1.3.1) tools (22) with GENCODE V30 as a reference and summarized at both gene and isoform levels. Duplication and GC content levels were estimated by Picard tools (v2.2.4). Quality control (QC) metrics were collected by RNA-seq QC (v1.1.8) (23).

Exploration of covariates and model selection

First, we performed a principal component analysis (PCA) on the normalized read count matrix to identify high-variance components that explained at least 1% of the variance. Correlation tests were performed between the selected PCs and known covariates from the QC metrics, and covariates with a false discovery rate (FDR) < 0.05 were used for the following steps. To select the final covariates, we first chose the covariates including cell type, stage and sex that are known to play a critical role as a 'base model'. We then applied an approach based on the Bayesian information criterion (BIC) to select the final covariates (24). We examined the BIC changes in the linear regression model after adding a new covariate, which will be included if it can improve the mean BIC by at least 4.

Deconvolution analysis

To estimate the cell composition in the sorted cells, we used single cell references of adult (25) and developing brains (26) with dtangle (27) to perform deconvolution analysis. Briefly, we first regressed out the selected covariates as described above. Then we utilized the expression levels of cell markers obtained from single-cell references and the residual matrix as input for dTangle (27) and quantified the cell type composition with a linear mixed model.

ChIP-seq data processing

H3K4me3, H3K27ac, H3K27me3 ChIP-seq and corresponding input files were aligned to human genome hg38. The resulting bam files were subsampled to the same sequencing depth and merged for each cell type. We called peaks using MACS with a smoothing window of 150bps (–shift -75 –extsize 150 –nomodel), FDR of 0.01 (-q 0.01) and input as control. For H3K27me3, we called broad peaks (–broad). Peaks overlapped with ENCODE blacklist regions[95] were discarded.

Chromatin states annotation

We implemented a multivariate Hidden Markov Model model (ChromHMM) (28) to systematically annotate the combinational effect of different histone modifications. The ChromHMM model is trained by virtually concatenating histone marks H3K4me3, H3K27ac and H3K27me3 in all three cell types that merged across all individuals that subsampled to uniform depths. Reads were shifted from 5′ to 3′ direction by 100 bp for all the samples. Read counts were then computed in 200 bp non-overlapping bins across the genome. Each bin was binarized into 1 or 0 by the Poisson model with a *P*-value threshold of 10^{-4}. We have trained the model with merged data using six states which captured all the key interactions from our data. Lastly, we obtained the chromatin states with the trained model and corresponding binarized files as input.

Hi-C data processing

Alignment and filtering

Hi-C data were aligned using the HiC-Pro strategy (29). Briefly, paired-end reads were mapped independently to the human genome hg38 using bowtie2 in stringent mode with parameters ('–very-sensitive -L 20 –score-min L,-0.6,-0.2 –end-to-end')(30). Then, the chimeric reads that failed to align were trimmed after ligation sites (MboI 'GATCGATC') and mapped to the genome. All the aligned reads from both ends were then merged based on read names and mapped to MboI restriction fragments using hiclib package (31). Next, self-circles, dangling ends, PCR duplicates and genome assembly errors were discarded. Samples of the same cell type were merged. We binned the interaction matrix at different resolutions and corrected it with iterative correction (ICE) for downstream analysis. We collected Hi-C specific quality control information for each technical replicate, including (i) percent of input chimeric reads, (ii) alignment summary from HiC-Pro, (iii) quality control from hiclib package, including self-circle, dangling ends, PCR duplicates, percent of *cis*/trans reads, (iv) slop, the slope of the linear regression between log scaled average interaction frequency and log scaled average genomic distance (100 kb–10 Mb, 100 kb resolution), (v) percent of contacts within between TADs (insulation region) (for TAD analysis).

Consistency between replicates

To determine the reproducibility across different replicates of our Hi-C data, we used HiCRep package (32). HiCRep stratified the interaction matrix by genomic distance and then determined the stratum adjusted correlation coefficient (SCC) to compare the similarities. We compared the biological replicates of neuron, fetal and glia samples at 100 kb resolution. The samples exhibit strong within-group correlation.

High-resolution compartment analysis

To annotate high-resolution A/B compartments for each of the different tissue and stage, we used a two-step strategy. First, we performed principal component analysis using a genome-wide interaction matrix at 200 kb. We compared the correlation between the resulting first principal component (PC1) and gene density of each bin, and reverse the sign if it's a negative correlation. Thus, we generated a genome-wide compartment score at low resolution. Next, for each chromosome, we used the CscoreTool (33) to annotate A/B compartments at 40 kb bin resolution. The conventional Principal Component Analysis (PCA) method of identifying compartments is a descriptive statistical method in which the biological meaning of the compartment score is unclear, and therefore compartment scores calculated from different Hi-C datasets may not be directly comparable. Conversely, the Cscore tool uses a statistical model which reflects the probability of a given genomic window of being in the A compartment in an individual cell. Furthermore, PCA is slow and memory-inefficient when applied to large interaction matrices, whereas the Cscore tool is specifically designed for fast and accurate compartment analysis in high resolution HiC data. We reversed the sign of the Cscore if it correlates negatively with the genome-wide PC1 score. We discard the chromosomes where the PC1 and Cscore have a low correlation (Pearson correlation < 0.5). In this way, we generated a high-resolution compartment annotation for each group.

To identify compartment switching, we convert the cscore difference between two tissues or stages into *z*-scores and get the corresponding *P*-value smaller than 0.01 bins as compartment switched loci. As aged adult glia samples are very similar to young adult glia samples, we used the two as biological replicates. We determined the standard deviation (sd0) of the cscore differences between the two. For every comparison, we divided cscore differences between conditions by the sd0, and the resulting z-score was subsequently converted to a *P* value, and adjusted for multiple testing (FDR). Only the cscore changes with FDR <0.05 and that have opposite signs were identified as differential compartments. We also identified switched compartments using PCA, in which the bin size was 200 kb, as opposed to the 40 kb bin used for the CscoreTool, where we calculated the difference in eigenvalues, and those that have opposite signs and are FDR significant (<0.05) for every pairwise comparison were identified as differential compartments.

We also analyzed the strength of the compartment by generating saddle plots using the cooltools package (https://github.com/open2c/cooltools/tree/master/cooltools). Briefly, intra-chromosome interactions were normalized and averaged for each genomic distance at 40kb bin. Then the distance normalized interactions were aggregated by the high-resolution compartment score.

To determine the association between chromosome compartment differences and epigenomic modification changes, we assessed the delta Cscore (Neuron -glia, or Neuron - fetal) and the delta ChromHMM annotation coverage for each bin (40 kb). Similarly, we also assessed the gene expression fold change, and the delta Cscore (determined by the Cscore

of the bin that TSS resides). We highlighted the genes with top positive and negative log fold changes between cell types.

We collected functional gene sets from (i) MSigDB 7.0 (34) and (ii) dysregulated genes in Huntington's Disease (35). To assess the function associated with the compartment changes, we determined the genes that the TSS located in the differential compartments. One-tailed Fisher exact tests with genome-wide protein-coding genes were used to test the enrichment and significance.

TAD analysis

Topological associated domains (TADs) were identified with Topdom (36) at 10K resolution and a 200 kb window size.

In order to quantify the dynamic of TADs during the development process as well as after CRISPR interference, we determined the insulation score (37) of all the shared TAD borders across different technical replicates. Read counts were then normalized with the trimmed mean of M-values (TMM) method (38). We performed a PCA on the normalized read count matrix for each assay to identify high-variance components that explained at least 1% of the variance. Correlation tests were performed between the selected PCs and known covariates, and covariates with FDR < 0.05 were used for the following steps. To select the final covariates, we first chose the covariates such as cell types and sex that are known to play a critical role for each assay as 'a base model'. We then applied an approach based on the Bayesian information criterion (BIC) to select the final covariates (24). We examined the BIC changes in the linear regression model after adding a new covariate, which will be included if it can improve the mean BIC by at least 4. In different comparisons across development, we used covariates including person ID, sex, pool, slope, percent of *cis*-reads and percent of contacts between TADs (insulation region). For CRISPR interference analysis, we used covariates including slope, percent of trans reads, percent of dangling ends, PCR duplicates, non-unique map reads.

With the selected covariates, the normalized read counts were modeled with the voomWithQualityWeights function from the limma package (v.3.38.3) (39), which utilizes both sample-level and observational-level weights. We subsequently perform the test against the contrast between tissues or between CRISPR treatment using a linear mixed model to account for repeated measurements (i.e. two brain regions per individual) in the dream function (40) of the variancePartition package (41).

In order to annotate the differential TAD borders, we determined the ChromHMM annotation, compartment score and insulation score across the 100 kb window up/downstream of the differential TAD borders at 10 kb bins. The side with a lower compartment score was set as upstream (–100k). We also collected functional gene sets from MSigDB 7.0 (34), and used one-tailed Fisher exact tests to test the enrichment and significance of the differential TAD borders associated genes.

Chromatin loop analysis

Chromatin loops were identified with both HICCUPS (42) and Fit-Hi-C (43) of merged Hi-C contacts for each tissue. For Fit-Hi-C, loops were called from 5k to 20k (by 1k) resolution. In order to get a consistent P cutoff, we used the P cutoff of FDR (Benjamini–Hochberg adjusted) <0.05 at 10 kb for different resolutions. After that, we get the chromatin loops that are reproducible in at least two different resolutions. For HICCUPS, chromatin loops were called using juicer HICCUPS with bin sizes iterated from 10 kb to 25 kb by 1kb intervals and parameters '-k VC_SQRT -p 1 -i 3'. Only reproducible loops were retained and the highest resolution of the overlapping loops was used. Lastly, loops were merged from the two methods.

In order to annotate differential loops, we determined the interaction counts at 20 kb resolution across all the technical replicates. Then we used the same pipeline as the differential TAD analysis to identify differential chromatin loops.

In order to annotate all the promoter-associated loops, we get all the promoters (1 kb of TSS) that within the chromatin loop anchors. We get the chromatin states at the promoter loci, as well as the chromatin states at the distal region. Then we assign the promoter and the distal region to the chromatin state that has the largest coverage.

We collected functional gene sets from MSigDB 7.0 (34), and human brain single-cell markers (25) and perform one-tailed Fisher exact tests to test the enrichment and significance of loop associated genes.

To determine the gene loops, we utilized the gene-code annotation (GENCODE V30), and we assigned an isoform as loop-isoform if both of the loop anchors overlapped with the exons within the isoform. To avoid the potential bias from gene length, we normalized the isoform-level gene expression into TPM, and determined the median non-loop isoform and the median loop isoform expression level.

Partitioned heritability analysis

We partitioned heritability for loop anchors to examine the enrichment of common variants in neuropsychiatric traits with stratified LD score regression (v.1.0.0)(44) from a selection of GWAS studies (45–51). Briefly, with the loop anchors, a binary annotation was created by marking all HapMap3 SNPs (52) that fell within the loop anchors and outside the MHC regions. LD scores were calculated for the overlapped SNPs using an LD window of 1cM using 1000 Genomes European Phase LD reference panel (53). The enrichment was determined against the baseline model (44).

Results

Neurons show weaker genome compartmentalization than glia and form stronger TADs, which emerge during fetal development

We performed *in situ* Hi-C (18) on nuclei isolated from *ex vivo* human fetal cortical plate tissue from 18–19 post-conception weeks (pcw) (2 unique donors, defined as early mid gestation fetal) and 23–24 pcw (2 unique donors, defined as late mid gestation fetal), and on neurons and glia sorted from the prefrontal cortex tissue from young (2 unique donors, 30–40 years of age) and old (4 unique donors, 80–100 years of age) adulthood (Supplementary Table S4). The 18–24 pcw developmental timeframe represents a period when neurons are completing their migration into the cortical plate (54) and extending their synaptic projections (55–57), thus transitioning towards functional maturity. After pooling reads from biological replicates, we obtained 1.2 billion unique *cis* contacts from fetal cortical plate tissue, and 1.6 and 1.8 billion from adult neurons and glia, respectively, producing ultra-deep 3D genome maps in primary human brain tissue across development (Supplementary Table S5). Glial (NeuN-) nuclei sorted

from the adult prefrontal cortex are more heterogeneous than the neuronal population, derived from a number of different non-neuronal cell types, including oligodendrocytes, astrocytes and microglia. To refine our analysis, we also investigated the 3D genome of *ex vivo* microglial cells, isolated from fresh human postmortem brain specimens (58) (donor information in Supplementary Table S4). Microglia are a specific glial subtype that, unlike other non-neuronal cells, do not originate from neural stem cells, and are considered to be the resident immune cells of the brain. Therefore, this approach enabled us to compare neurons to a functionally and developmentally distinct cell type in the brain, allowing us to examine lineage specific differences in 3D genome structure.

We initially measured the similarities of Hi-C matrices across biological replicates using HiCRep (32), including the microglial HiC dataset for comparison. As expected, the four cell/tissue types, including neuron, glia, fetal cortical plate and microglia form four separate clusters (Supplementary Figure S1A). To further assess the similarity between the groups, we compared the HiCRep correlation coefficients between groups (Figure 1A). Adult neurons and microglia are most distinct from each other, and glia (NeuN-) show a stronger correlation with neurons. Deconvolution analysis on glial RNAseq data using the expression levels of cell markers obtained from single cell references in the adult brain showed that the glia (NeuN-) population is mostly enriched in oligodendrocytes (Supplementary Figure S1B). As oligodendrocytes emerge from neural stem cells, they are developmentally more closely related to neurons than microglia, therefore our analysis reveals biologically relevant differences in the 3D genome. Although the difference between the fetal cortical plate and adult neurons is statistically significant (NeuronvsFetal versus EarlyFetalvsLateFetal P value = 1.396-e^{-45}), it is less pronounced than the cell type specific difference within the adult brain (Figure 1A). Deconvolution analysis on RNA-seq data from the fetal cortical plate using the expression levels of cell markers obtained from single cell references in the developing brain showed that the fetal cortical plate is mostly enriched in excitatory and inhibitory neurons, similar to the cell type composition in the adult neuronal population (Supplementary Figure S1B), and a smaller number of neural progenitors, such as radial glia and intermediate progenitor cells, but very few glia (Supplementary Figure S1C). This result corroborates a previous study showing that the fetal cortical plate is enriched in neurons (59). Therefore, we consider the Hi-C data derived from the cortical plate as representative of the 3D genome of developing fetal neurons. Altogether, we infer that although there may be large scale differences in the 3D genome between distinct cell types in the adult brain, the developmental differences between neurons in the fetal cortical plate and adult neurons may be subtler, involving fine-tuning of chromatin interactions rather than broad changes in 3D genome organization.

We proceeded to determine the intra-chromosomal chromatin interaction frequencies across genomic distance to obtain insights on the differences in the spatial organization of chromatin across our samples. Adult neurons have a higher density of contacts <1 MB than glia, followed by a steep decline in chromatin interaction frequencies at distances >1 MB, a pattern that emerges in the fetal cortical plate (Figure 1B). To eliminate potential technical bias, we also determined the interaction frequency distributions across genomic distance in previously published independent fetal cortical plate (12) and adult neuron and glia Hi-C datasets (15). We found that interaction frequency distributions are very reproducible across biological replicates from different studies (Supplementary Figure S1D, E). We show the read count distributions across different genomic distance ranges for our data and the previously published data cited above in a supplementary table (Supplementary Table S6). Overall, chromatin interaction patterns are similar between early and late fetal cortical plate samples, and between young and old adult brains for neurons and glia, respectively. Furthermore, as shown in our matrix reproducibility analysis with HiCRep (32), the early and late fetal samples cluster together, and the neuronal and glial samples from young and old adult brains cluster together (Supplementary Figure S1A). Therefore, in order to increase statistical power, most of the subsequent analyses were performed on three merged pools of Hi-C data: fetal cortical plate, neurons and glia.

We inferred that the steep decline in chromatin interaction frequencies at genomic distances >1 MB in neurons, a pattern that emerges during fetal development, may correspond to a disruption of long-range compartmental interactions. Indeed, we find that glial HiC heatmaps reveal more prominent plaid patterns than neuronal heatmaps, indicative of increased compartmentalization (Figure 1C). We used the CscoreTool (33) to identify A/B compartments at a 40 kb resolution, which uses a statistical model that predicts the probability of a given genomic window of belonging to an A compartment, with a positive cscore corresponding to an A compartment and a negative cscore corresponding to a B compartment. We detect more frequent A/B compartment switching in glial cells compared to neurons, especially in microglia, as highlighted in the expanded heatmap (Figure 1D), showing that compartmental interactions are disrupted in neurons. Another observation that shows the disruption of local compartmentalization in neurons is the lower frequency of overlap between compartment borders and TAD boundaries relative to glia (Figure 1E). We then quantified the strength of intra-chromosomal A–A and B–B compartment interactions across genomic distance to compare compartmentalization patterns across both short-range and long-range genomic interactions. Interestingly, both the fetal cortical plate and adult neurons display stronger long-range (>10 MB) A–A than B–B compartment interactions when compared to glia and microglia (Figure 1F, G). In contrast, mid-range (1–10 MB) contacts in both fetal cortical plate and adult neurons show weakened A-A interactions, whereas B-B compartment interactions are stronger. We were also able to reproduce our results in the previously mentioned independent published fetal cortical plate (12) and adult neuron and glia (15) HiC datasets, in which similar patterns of A-A and B-B compartment interactions across genomic distance were observed (Supplementary Figure S1F, G).

Initial 3C based studies described TADs as smaller building blocks of the 3D genome that reside within broader compartments (5,6), However later studies contested this static view as it was found that the relationship between TADs and compartments is dynamic, whereby the proposed mechanism of loop extrusion strengthens TADs but weakens compartments (60,61). As we detected a disruption of compartmental interactions in neurons, we inferred that this could imply the formation of stronger TADs, coinciding with the loop extrusion model. We therefore determined the distributions of insulation scores across our samples within 1 MB genomic intervals, as 0–1 MB contacts have been defined as intra-TAD

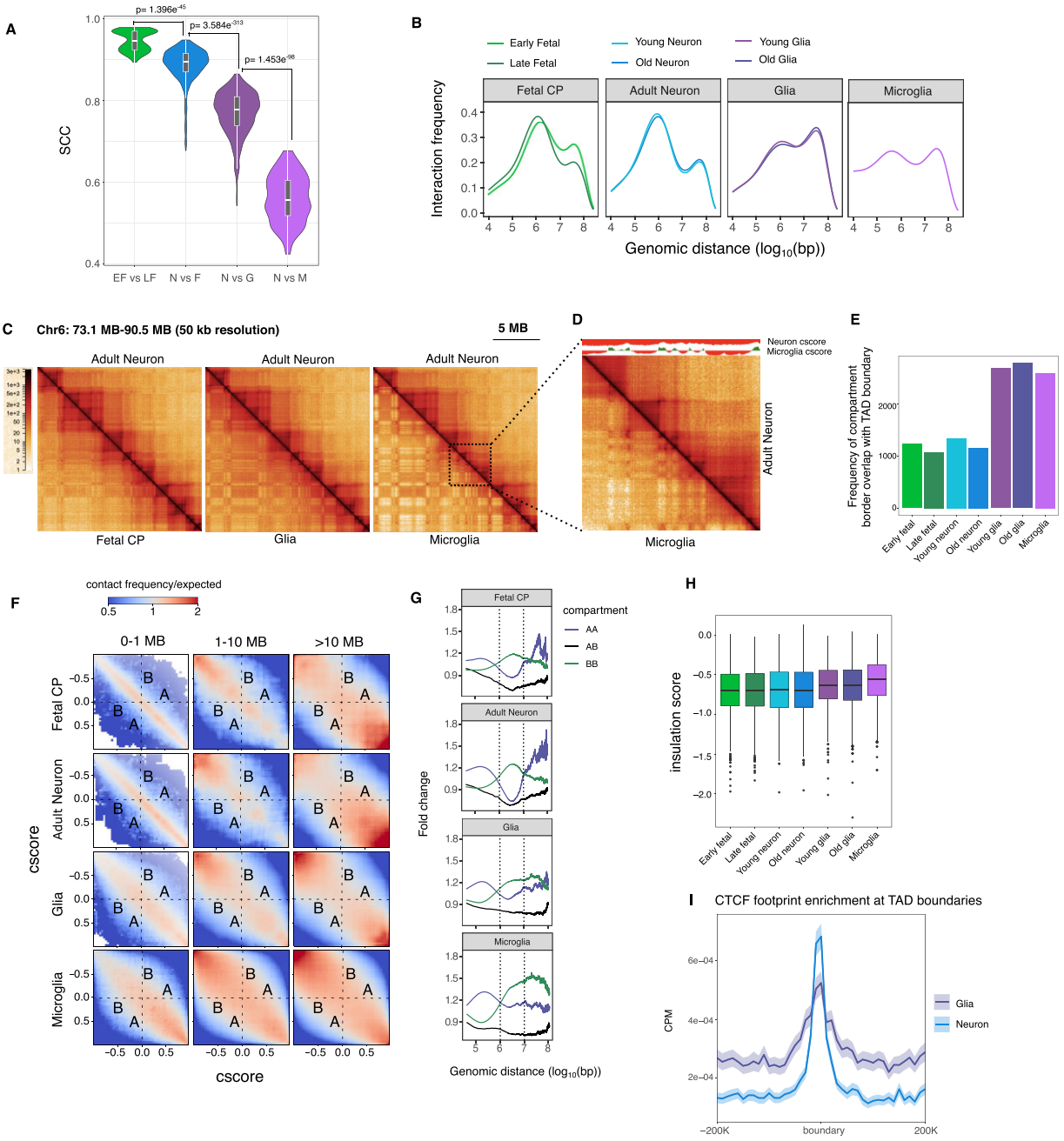

Figure 1. Neurons show weaker genome compartmentalization than glia and form stronger TADs, which emerge during fetal development. **(A)** Boxplot showing correlations between groups of HiC datasets measured by the stratum adjusted correlation coefficient (SCC) using HiCRep and the statistical significances (t test) of the differences between inter-group correlations. EF: Early Fetal, LF: Late Fetal, F: Fetal, N: Adult Neuron, G: Adult Glia, M: Microglia. **(B)** Kernel density estimation plots showing intra-chromosomal chromatin interaction frequency versus genomic distance ($\log_{10}$(bp)). **(C)** Snapshots of contact matrices from the HiGlass 3D genome browser comparing merged HiC data from adult neurons (NeuN + cells) versus fetal cortical plate tissue (left), adult neurons versus glia (NeuN- cells) (middle) and adult neurons versus microglia (CD45 + CD11b + cells) (right), Chr6:73.1 MB-90.5 MB, at 50 kb resolution. Genomic distance scale bar (5 MB) is shown on the upper right of the panel. **(D)** Zoomed in matrix of a 5 MB region showing differences in compartmentalization between neurons and microglia. tracks of cscores are displayed above. Negative cscores (corresponding to the B compartment) are red, and positive cscores (corresponding to the A compartment) are green. **(E)** Frequency of compartment/TAD border overlap across different cell types/stages. Compartment borders within 100 kb of TAD boundaries are considered as overlapping. **(F)** Saddle plots generated by cooltools displaying intra-chromosomal A–A and B–B interactions in the merged contact maps of fetal cortical plate cells, adult neurons, glia and microglia at three genomic distance ranges (0–1, 1–10 and > 10 MB) between 40 kb bins ranked by their compartment scores (determined using the CscoreTool). **(G)** Frequency of A–A, A–B and B–B compartment interactions across genomic distance ($\log_{10}$(bp)) expressed as fold enrichment above all compartment interactions. The dashed lines correspond to the different genomic distance ranges we used in the saddle plots (0–1, 1–10, >10 MB). **(H)** Genome-wide insulation score distributions (within 1 MB genomic intervals) across different cell types/stages. Early fetal versus young glia: FDR = 9.055e-^{24}, early fetal versus old glia: FDR = 1.0051e-^{19}, early fetal versus microglia: FDR = 2.111e^{-69}, late fetal versus young glia: FDR = 2.0023e^{-23}, late fetal versus old glia: FDR = 2.373e^{-19}, late fetal versus microglia: FDR = 1.638e^{-68}, young neuron versus young glia: FDR = 1.078e^{-18}, young neuron versus old glia: FDR = 1.21e^{-15}, young neuron versus microglia: FDR = 4.236e^{-58}, old neuron versus young glia: FDR = 3.381e^{-18}, old neuron versus old glia: FDR = 4.218e^{-15}, old neuron versus microglia: FDR = 4.236e^{-58} (Wilcox test). **(I)** CTCF footprint (obtained using TOBIAS (V1.01) on ATACseq data) distributions around TAD boundaries.

interactions (62), to verify if neurons have stronger TADs. We found increased insulation within neurons relative to glial cells (Figure 1H), with the fetal cortical plate and adult neurons showing statistically significant decreases in insulation scores (more insulated) relative to glia and microglia (Supplementary Table S7). To gain some mechanistic insight into the weakened compartmentalization and stronger TADs in neurons, we performed a transcription factor footprinting analysis (63,64) on ATAC-seq (65) data generated from our adult neuron and glia samples to determine the distributions of CTCF binding sites. Interestingly, while glia have a higher proportion of OCRs (open chromatin regions) enriched in CTCF footprints (29 845/134 253 in glia and 20 179/217 319 in neurons), there is a higher enrichment of CTCF footprints specifically at TAD boundaries in neurons (Fisher's exact test, odds ratio = 2, *P*-value = 1.04×10^{-43}), which could help explain the increased strength in chromatin insulation in neurons (Figure 1I). We found that 70% of our neuron CTCF footprint peaks (10 169/14 466) overlap with CTCF ChIPseq peaks from ENCODE hESC-derived neurons, thus validating their biological relevance (Supplementary Figure S1H). We also analyzed RNAseq data and found that while CTCF, structural components of cohesin such as STAG1, STAG2 and SMC3, cohesin loading factor NIBPL, and cohesin release factor WAPL are all downregulated in neurons relative to glia, RAD21 is slightly more highly expressed in neurons than in glia (logFC 0.317, FDR = 4.2×10^{-9}) (Supplementary Table S8). Interestingly, a recent study that combined data from microscopy and HiC (66) showed that upregulating RAD21, but not other cohesin subunits, results in a 'beads-on-a-string' chromatin configuration indicative of increased loop extrusion, which disrupts compartmentalization and significantly decreases long range contacts, similar to the patterns we observe for neurons relative to glia. Also, another recent study showed that RAD21 is involved in the regulation of a subset of large neurodevelopmental genes in mouse neurons (67). Altogether, we found that neurons show a loss of fine scale genome compartmentalization and stronger TADs, which emerge during fetal development.

Neuronal differential compartments tend to be repressive and are mostly established during fetal development

Having shown differences in compartment level structure between neurons and glial cells, we then investigated the functional significance of these differences. Firstly, we measured the concordance of A/B compartments across our samples by quantifying the Pearson correlations between cscores (Supplementary Figure S2A). Microglia show the weakest A/B compartment concordance with adult neurons. Fetal cortical plate shows the strongest A/B compartment concordance with adult neurons, suggesting that a large proportion of compartments in adult neurons are formed during fetal development. We then identified differential compartments by performing pairwise comparisons between our merged HiC datasets quantifying the number of loci that switch from A-to-B and B-to-A. As compartments can differ in size, potentially biasing the results, we identified differential compartments using both CscoreTool at a bin size of 40 kb, as well as the conventional principal component analysis (PCA) approach at a bin size of 200 kb, and determined the correlation between the results. There is strong correlation between both methods, and we detect broader genome-wide differences in A/B compartments between distinct cell types in the adult brain than across neural development from fetal to adult (Figure 2A). Furthermore, there is a stronger shift towards B type compartments in neurons during development, also shown in a plot that describes the genome coverage of switched compartments for all of our pairwise comparisons (Supplementary Figure S2B). Our differential compartment analysis can be replicated in previously published fetal cortical plate (12) and adult neuron and glia HiC data (15) (adult Neuron versus glia: $\rho = 0.851$; $P < 10^{-16}$, adult neuron versus fetal CP: $\rho = 0.685$; $P < 10^{-16}$) (Supplementary Figure S2C). Altogether, the compartments that distinguish neurons from non-neuronal lineages are mostly established during fetal development and tend towards the repressive B type rather than the active A type.

As there could be experimental biases associated with compartment identification, we next measured the density of histone modifications obtained from ChIP-seq data (Supplementary Figure S2D) from the same donors to validate that differential compartments are associated with expected differences in regulatory epigenetic signatures. Specifically, we generated scatterplots to correlate the shifts in cscore values of individual compartments with shifts in the enrichment of chromatin states (defined by ChromHMM) that correspond to active enhancer (H3K27ac), polycomb repressed chromatin (H3K27me3), active promoter (H3K4me3, H3K27ac) and non-active promoter (H3K4me3, H3K27me3). A positive shift in the cscore implies an increased probability of a compartment being A type, whereas a negative shift in the cscore implies an increased probability of a compartment being B type. Our adult neuron versus glia and adult neuron versus fetal cortical plate analyses both show that an increased shift towards an A compartment is associated with an increased enrichment of active enhancers (adult neuron versus glia: $\rho = 0.383$; $P < 10^{-16}$, adult neuron versus fetal CP: $\rho = 0.165$; $P = 2.89e^{-229}$) and active promoters (adult neuron versus glia: $\rho = 0.199$; $P = 8.33e^{-175}$, adult neuron versus fetal CP: $\rho = 0.0892$; $P = 5.9e^{-39}$) whereas an increased shift towards a B compartment is associated with an increased enrichment of polycomb repressed chromatin (adult neuron versus glia: $\rho = -0.305$; $P < 10^{-16}$, adult neuron versus fetal CP: $\rho = -0.0999$; $P = 5.17e^{-79}$) and non-active promoters (adult neuron versus glia: $\rho = -0.377$; $P < 10^{-16}$, adult neuron versus fetal CP: $\rho = -0.101$; $P = 1.62e^{-24}$) (Figure 2B). We also highlight some biologically relevant examples from HiC matrices where compartment switching and the relationship to epigenetic changes is evident (Figure 2C). For Neuron A/Glia B we show *KCNJ6*, a gene that encodes a G protein coupled potassium channel implicated in neuronal circuit activity. For Glia A/Neuron B we show *SALL1*, a gene expressed in oligodendrocytes in postnatal stages. For Fetal A/Neuron B we highlight *BMP7*, a gene that promotes neurogenesis. Given that the process of neurogenesis is active in the fetal cortical plate but suppressed during adulthood in healthy brains, *BMP7* may be likely to shift towards a repressive B compartment during neural development. Overall, our analysis confirms that differences in 3D genome structure at the compartment level are correlated with changes in the linear epigenome.

We then looked at gene expression changes associated with neuron versus glia and adult neuron versus fetal cortical plate differential compartments and found that a more positive shift in the cscore corresponds to an increase in gene

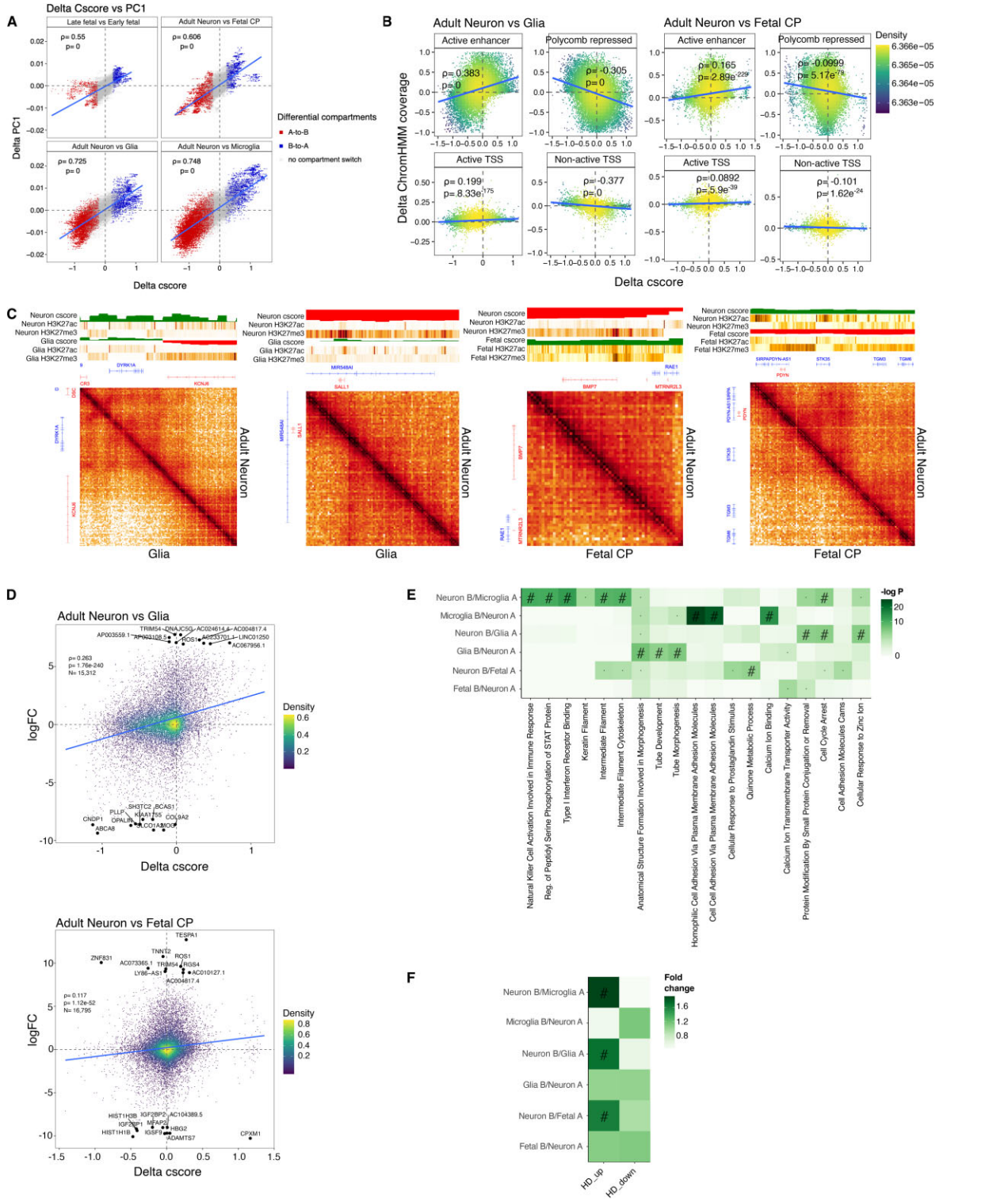

Figure 2. Neuronal differential compartments tend to be repressive and are mostly established during fetal development. **(A)** Spearman correlations between two methods for differential compartment analysis, PC1 (200 kb bin) versus CscoreTool (40 kb bin). $P < 10^{-16}$ (FDR significant). **(B)** Scatterplots showing Spearman correlations between change in compartment score (delta cscore) per 40 kb bin and change in chromatin state enrichment (delta ChromHMM coverage) comparing adult neurons versus glia and adult neurons versus fetal cortical plate. **(C)** HiC matrices with tracks of cscores (negative cscores, corresponding to the B compartment, are red, and positive cscores, corresponding to the A compartment, are green) and H3K27ac and H3K27me3 densities to highlight examples of compartment switching that correlate with epigenetic changes. **(D)** Scatterplots showing Spearman correlations between change in compartment score (delta cscore) and change in gene expression (logFC) comparing adult neurons versus glia and adult neurons versus fetal cortical plate. Genes whose expression are the most strongly upregulated or downregulated in switched compartments are highlighted in each scatterplot. **(E)** GO term enrichment in differential compartments. ·, nominally significant ($P < 0.05$); #, significant after FDR (Benjamini and Hochberg) correction (FDR < 0.05). **(F)** Association of differentially regulated genes in Huntington's disease with differential compartments. HD_up: genes upregulated in Huntington's disease, HD_down: genes downregulated in Huntington's disease. ·, nominally significant ($P < 0.05$); #, significant after FDR (Benjamini and Hochberg) correction (FDR < 0.05).

expression and a more negative shift in the cscore corresponds to a decrease in gene expression, as expected (Figure 2D). We then identified genes with the largest fold change in expression in differential compartments. Among genes that are most strongly down-regulated in neuron versus glia differential B compartments, we find *PLLP, SH3TC2* and *MOG,* which are involved in myelination, a key function of oligodendrocytes, and *OPALIN,* which regulates oligodendrocyte differentiation. Among genes that are most strongly down-regulated in adult neuron versus fetal neuron differential B compartments we find *HIST1H3B* and *HIST1H1B,* genes encoding replication-dependent histone proteins of the H3 and H1 families, respectively, and *IGSF9,* a gene involved in axon guidance and predicted to act upstream of or within dendrite development and regulation of synapse organization. It is possible that neurons in the cortical plate within the 18–24 pcw timeframe have not yet become post-mitotic and therefore show residual expression of replication dependent histone proteins, whereas adult neurons are completely post-mitotic and therefore repress these genes through A-to-B compartment switching. The repression of *IGSF9,* a gene involved in early neurodevelopmental processes, also shows the functional relevance of A-to-B compartment switching in neuronal maturation. As previously mentioned, young and old adult samples show strongly correlated HiC matrices, so we can consider them as biological replicates. Therefore, we also performed pairwise differential compartment analyses between the merged fetal cortical plate data and the young and old adult neuron HiC datasets separately to test the robustness of our analysis. The differential compartments from fetal versus young adult neuron and fetal versus old adult neuron are consistent with each other ($\rho = 0.906$, $P < 10^{-16}$) (Supplementary Figure S2E). We then measured gene expression changes associated with young adult neuron versus fetal and old adult neuron versus fetal differential compartments, and obtain reproducible results, which correlate strongly with our merged adult neuron versus fetal analysis Supplementary Figure S2F).

In order to understand the biological significance of differential compartments, we performed gene set enrichment analysis (Figure 2E). Microglia versus neuron differential compartments show functionally relevant pathways. Microglia B/neuron A compartments are enriched for processes such as cell-to-cell adhesion and calcium ion binding, which are important for neuronal connectivity and activity. Conversely, Neuron B/microglia A compartments are enriched for pathways related to immune function, which correlates with the role of microglia as the immune cells of the brain. However, molecular pathway analysis in adult neuron versus glia and adult neuron versus fetal neuron differential compartments fails to reveal similarly significant pathways that are functionally relevant, which could be attributed to the heterogeneity of the glial population and fewer differential compartments between fetal and adult neurons.

The prevalence of differential B compartments in adult neurons that are enriched for polycomb repressed chromatin and non-active promoters suggests an important role for the 3D genome in gene suppression. Recent studies show the importance of the polycomb repressive complex 2 (PRC2) in the central nervous system (68–70). In particular, PRC2 was shown to have a neuroprotective role, as depletion of PRC2 in mouse neurons leads to upregulation of specific genes that promote neurodegeneration (69). Furthermore, 20–30% of these genes were shown to overlap with genes that are upregulated in the postmortem brains of patients suffering from Huntington's disease (HD), a well-known neurodegenerative disorder (35,71,72). Therefore, we hypothesized that differential B compartments in adult neurons, which we show to be differentially enriched in polycomb repressed chromatin and non-active promoters, might be enriched for genes that are implicated in neurodegeneration, highlighting the role of the polycomb associated chromatin interactome in suppressing genes to ensure neuronal survival. Next, we determined whether genes that were shown to be differentially upregulated in HD patients (35), are significantly associated with differential B compartments in adult neurons. Indeed, we found that Neuron B/Microglia A, Neuron B/Glia A and Neuron B/Fetal A compartments are all significantly associated with genes that are upregulated in Huntington's disease (Figure 2F). Therefore, the polycomb associated chromatin interactome in adult neurons may play a role in suppressing genes that are potentially neurodegenerative when activated.

Differential TAD boundaries in neurons are located in proximity to active genes that drive neurodevelopmental processes and are formed during fetal development

Most TADs are considered to be cell type invariant features of the 3D genome. However, little is known about cell type specific TADs and their relationship to gene regulation. Given that we observed a higher density of short range (<1 MB) interactions in neurons compared to glia, which correlates with weaker compartmentalization and stronger TADs, we inferred that this could be partially due to the presence of neuron specific TAD boundaries that insulate local chromatin interactions. Using the insulation score method to examine regions that are significantly more insulated in neurons relative to glia (–0.5 $\log_2$FC insulation score in 10 kb bins within 200 kb genomic interval, FDR < 0.05), we identified 529 differential TAD boundaries (Supplementary Table S9). These regions show similar levels of insulation in the fetal cortical plate, suggesting that differential TAD boundaries form during early development and are maintained throughout adulthood (Figure 3A). To gain insight into the epigenetic regulation associated with differential TADs in neurons, we determined the density of active enhancer (H3K27ac), polycomb repressed chromatin (H3K27me3), active promoter (H3K4me3, H3K27ac), and non-active promoter (H3K4me3, H3K27me3) states across differential and cell type invariant TAD boundaries (Figure 3B). Compared to cell type invariant TAD boundaries, differential TAD boundaries in neurons show a stronger enrichment of active promoter states relative to glia, as well as an asymmetric pattern of active enhancer enrichment downstream of the boundary. Conversely, when examined in glia, these same regions are enriched for non-active promoter states. Accordingly, we found that differential TAD boundaries in adult neurons are significantly enriched for neuronal gene expression relative to all TAD boundaries (Fisher's exact test, odds ratio = 1.186, P-value = $1.33e^{-06}$).

Genes positioned near differential TAD boundaries in neurons (Supplementary Table S10) are strongly enriched for processes related to neural development, such as cell-to-cell adhesion and synapse organization (Figure 3C). In the vicinity of strongly differential TAD boundaries (at least -1 logFC insulation) we find contactin-associated protein (CASPR) genes such as *CNTNAP2* (Figure 3D, E) and *CNTNAP5*

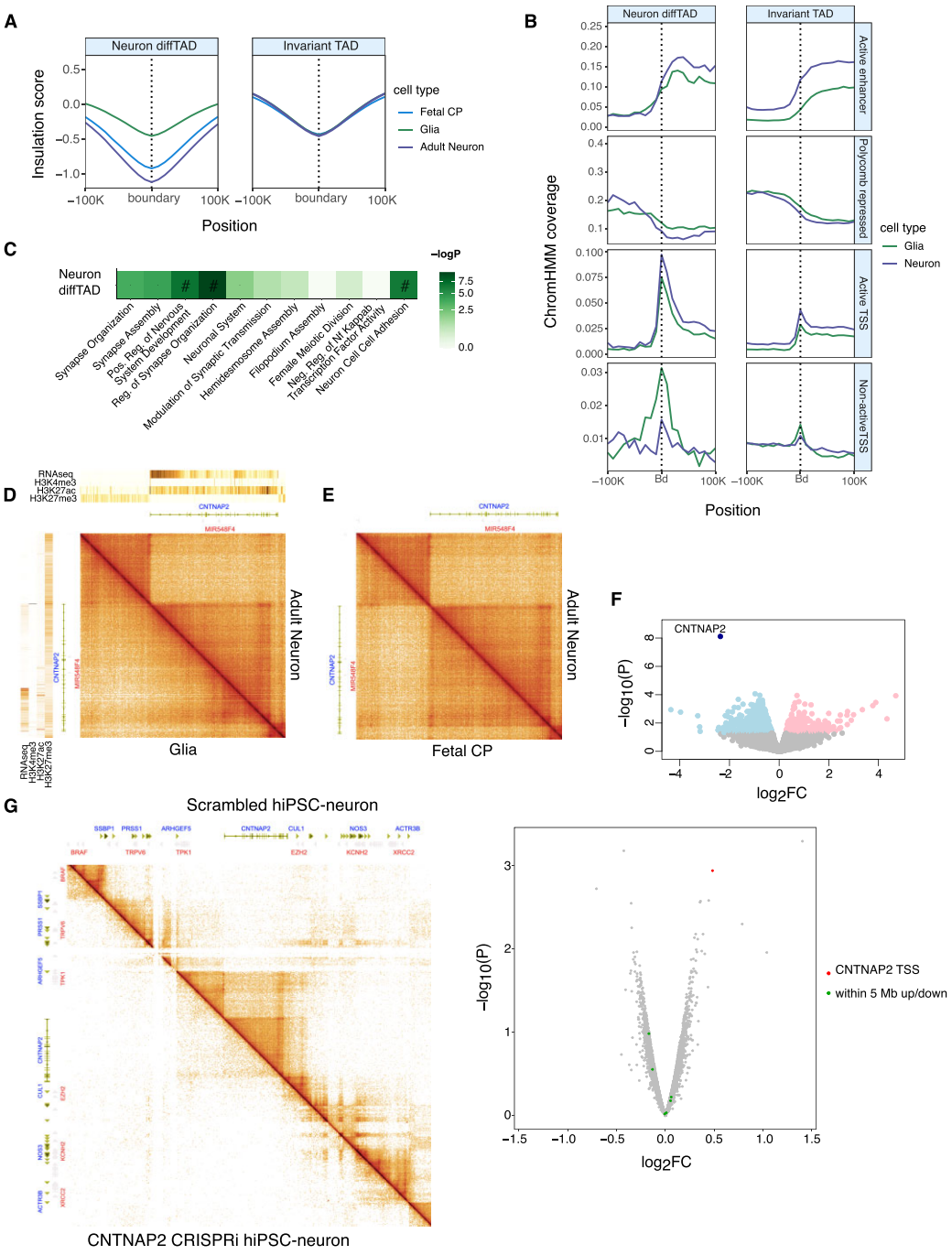

Figure 3. Differential TAD boundaries in neurons are located in proximity to active genes that drive neurodevelopmental processes and are formed during fetal development. **(A)** Insulation score distributions of fetal cortical plate, neuron and glia across neuronal differential TAD boundaries and invariant TAD boundaries. The insulation score distribution displayed for neuron diffTADs is calculated from the average of the insulation score distributions across all neuronal differential TAD boundaries. The differential TAD boundary analysis was performed within a genomic window of 200 kb calculating the insulation scores within 10 kb bins. If the insulation score fold difference in neurons within that 200 kb window was at least –0.5 log2FC compared to glia and statistically significant (FDR < 0.05), then it was defined as a neuronal differential TAD boundary. **(B)** Density of neuron and glia specific chromatin states across neuronal differential TAD boundaries and invariant TAD boundaries: active enhancer (H3K27ac), polycomb repressed (H3K27me3), active TSS (H3K4me3, H3K27ac), non-active TSS (H3K4me3, H27me3) Bd:Boundary. **(C)** GO terms associated with genes in the proximity of neuronal differential TAD boundaries. ·, nominally significant (P < 0.05); #, significant after FDR (Benjamini and Hochberg) correction (FDR < 0.05). **(D)** Snapshot of the *CNTNAP2* locus from the HiGlass 3D genome browser showing HiC contact maps (10 kb resolution) in neurons and glia along with RNA-seq and ChIP-seq of H3K4me3, H3K27ac and H3K27me3 from the respective cell types. **(E)** Snapshot of the *CNTNAP2* locus from the HiGlass 3D genome browser showing Hi-C contact maps (10 kb resolution) in fetal cortical plate and adult neurons. **(F)** Volcano plot of significance ($-\log_{10}(P)$) versus fold change ($\log_2$FC) in expression in *CNTNAP2* CRISPRi versus scrambled hiPSC derived neurons. Points representing genes reaching nominal significance in the DEG analyses are shown in pink or light blue (up-regulated and down-regulated, respectively), and the gene reaching significance after correcting for multiple testing (FDR < 0.05) shown in dark blue with the gene name (*CNTNAP2*). **(G)** HiC heatmaps of *CNTNAP2* CRISPRi (left) versus scrambled (right) hiPSC derived neurons and volcano plot of significance ($-\log_{10}(P)$) versus fold change ($\log_2$FC) in insulation score in *CNTNAP2* CRISPRi versus scrambled hiPSC derived neurons. Other TAD boundaries 5 MB upstream/downstream (shown in green) of the *CNTNAP2* TSS do not differ in their insulation levels from the rest of the genome-wide loci (Kolmogorov–Smirnov test $P = 0.849$, fail to reject null hypothesis).

(Supplementary Figure S3A), protocadherin genes such as *PCDH10* and *PCDH7* (Supplementary Figure S3B), and *FLRT2* (Supplementary Figure S3C), all of which encode cell-to-cell adhesion molecules that are crucial for neuronal connectivity. Interestingly, we also find lincRNA encoding genes in the vicinity of strongly differential TAD boundaries, such as *LINC00632*, which is associated with panhypopituitarism, an intellectual development disorder, and *LINC01322* (Supplementary Figure S3D), which has recently been shown to shape the gene expression program towards neurogenesis (73). Taken together, our data suggests that differential TAD boundaries in neurons are formed in early development, are maintained throughout adulthood, and are associated with transcription up-regulation of both protein coding and non-coding RNAs implicated in neurodevelopmental processes. When we apply the differential TAD boundary analysis to adult neuron versus fetal cortical plate datasets, we find fewer differential boundaries (164) (Supplementary Table S11), suggesting more subtle differences during neural development. Our differential TAD boundary analysis can be replicated in previously published fetal cortical plate (12) and adult neuron and glia HiC data (15) (adult neuron versus glia: $\rho = 0.801$; $P < 10^{-16}$, adult neuron versus fetal CP: $\rho = 0.58$; $P < 10^{-16}$ (Supplementary Figure S3E).

To determine if the formation of a differential TAD boundary is coupled to transcription initiation, we performed CRISPR-interference (CRISPRi) on *CNTNAP2* in hiPSC derived NPCs. Specifically, we recruited dCas9-KRAB to the TSS of *CNTNAP2* to induce repressive histone modifications that would prevent gene activation during differentiation (Supplementary Figure S3F). The *CNTNAP2* CRISPRi and control (scrambled gRNA) NPCs were then differentiated into neurons. Analysis of RNA-seq data in *CNTNAP2* CRISPRi versus control differentiated neurons showed highly significant downregulation only for *CNTNAP2* ($\log_2$FC$= -2$, *P*-value $= 1 \times 10^{-8}$), attesting to the specificity of the knockdown experiment (Figure 3F) (Supplementary Table S12). Performing a genome wide analysis of changes in TAD insulation scores in *CNTNAP2* CRISPRi versus control, revealed a significant decrease in insulation at the *CNTNAP2* TSS ($\log_2$FC $= 0.5$, *P*-value $= 0.001$) (Figure 3G) (Supplementary Table S13). To further validate the specificity of the experimental result, we also investigated other TAD boundaries 5 MB upstream and downstream of the *CNTNAP2* TSS associated boundary and found that their insulation levels do not differ from other genome wide loci between the CRISPRi and scrambled control experiments (Kolmogorov–Smirnov test, $P = 0.849$). Therefore, using *CNTNAP2* as a candidate gene, we show that formation of a differential TAD boundary is correlated with TSS activation.

Re-wiring of chromatin loops during neural development is associated with transcriptional and functional changes

We proceeded to analyze the 3D genome at a higher resolution to investigate changes in regulatory chromatin loops during human brain development. Firstly, we found that loops cluster strongly according to cell type, showing many differences between neurons and glia, but few differences between young and old adult brains (Figure 4A). Conversely, we find more differential loops between fetal cortical plate and adult neurons, demonstrating that there are fine scale changes in neuronal 3D genome organization between the mid-gestation period of cortical development and young adulthood. We include the numbers of loops that are unique versus shared across our merged fetal cortical plate, and adult neuron and glia datasets (Supplementary Figure S4A). We also correlated the fold change in read counts at the differential loop anchor regions in our data with the read counts at the same coordinates in the previously published fetal cortical plate (12) and adult neuron and glia HiC data ((15) to determine if the cell type specific and neurodevelopment specific differences in chromatin looping strength can be replicated. While not as robust as the differential compartment and differential TAD comparisons described previously, we nonetheless detect strong correlations (adult neuron versus glia: $\rho = 0.696$; $P < 10^{-16}$, adult neuron versus fetal CP: $\rho = 0.536$; $P < 10^{-16}$) (Supplementary Figure S4B).

To obtain insights into neurodevelopmental disease mechanisms, we performed stratified LD score regression to determine the heritability for complex traits and psychiatric disorders within differential loops. Differential loops in both fetal cortical plate and adult neurons are significantly associated with SCZ and bipolar disorder (BD), while only fetal differential loops are associated with autism (Figure 4B). Unlike SCZ and BD, whose symptoms emerge during early adulthood, the symptoms of autism emerge during childhood. Our findings indicate that autism may, in part, be caused by disruptions to regulatory interactions during early brain development.

In order to define the active versus repressive chromatin interactome, we next classified loops into two groups; those that are linked to active (H3K4me3, H3K27ac) promoters, and those that are linked to non-active (H3K4me3, H3K27me3) promoters. We assigned chromatin states to distal loop anchors and, as expected, found that active promoters have a significantly higher probability of interacting with active enhancers (H3K7ac), relative to other chromatin states (Supplementary Figure S4C). Relative to other chromatin states, non-active promoters have a significantly higher probability of interacting with distal polycomb repressed elements (H3K27me3), which we define as repressors. When we compared the proportion of loops that are classified as enhancer-promoter loops across cell types, we found a higher occurrence of enhancer-promoter loops in adult neurons (968 loops) relative to both fetal cortical plate (Fisher's exact test, odds ratio $= 4.46$, *P*-value $= 4.4e^{-304}$) and glia (Fisher's exact test, odds ratio $= 2.5$, *P*-value $= 5e^{-171}$) (Figure 4C). We also found a higher occurrence of repressor-promoter loops in both fetal (155 loops) and adult neurons (214 loops) relative to glia (Fisher's exact test, odds ratio $= 2.11$, *P*-value $= 1.4e^{-26}$ (fetal cortical plate relative to glia), odds ratio $= 2.45$, *P*-value $= 4e^{-42}$ (adult neurons relative to glia)) (Figure 4C). We also quantified the size distributions of enhancer-promoter and repressor-promoter loops and found that repressor-promoter loops tend to occur across larger genomic distances than enhancer-promoter loops (Supplementary Figure S4D). Altogether, our results suggest a cell type specific and age-dependent increase in distal enhancer usage for the regulation of active genes in neurons. In addition, we find a putative role for distal repressors in maintaining promoters in a non-active state throughout neural development.

We then explored the biological pathways associated with differential loops (Supplementary Figure S4E, F). As expected, enhancer-promoter loops that are specific to adult neurons are associated with higher gene expression in adult neurons,

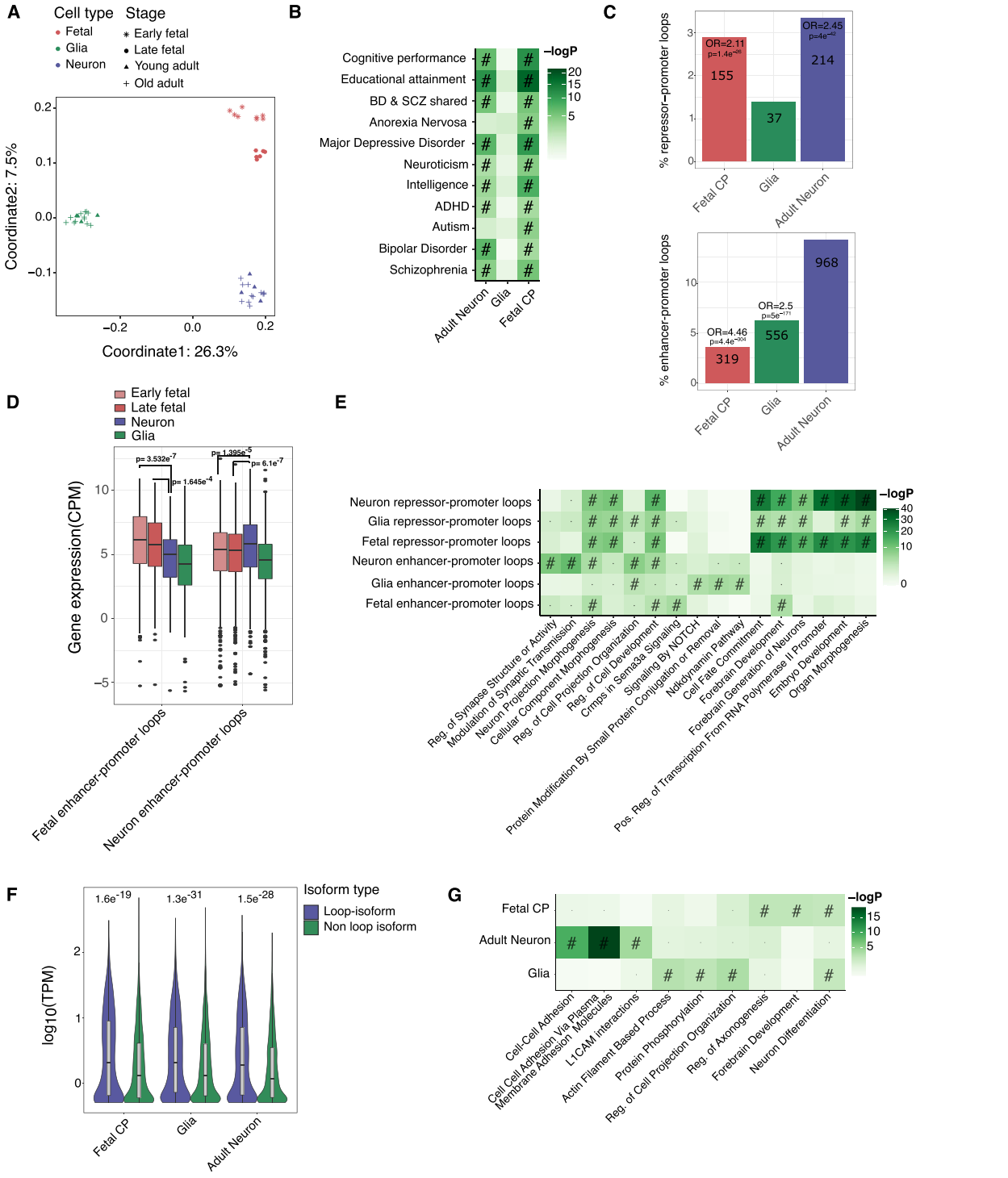

Figure 4. Re-wiring of chromatin loops during neural development is associated with transcriptional and functional changes. **(A)** Multidimensional scaling plot showing differential loops between different cell types and developmental stages (% variance explained). **(B)** Stratified LD score regression showing the heritability for complex traits and psychiatric disorders within regions associated with differential loops. ·, nominally significant ($P < 0.05$); #, significant after FDR (Benjamini and Hochberg) correction (FDR < 0.05). **(C)** Proportion of loops classified as enhancer-promoter (H3K27ac linked to H3K4me3/H3K27ac) or repressor-promoter (H3K27me3 linked to H3K4me3/H3K27me3). Enhancer-promoter frequency in adult neurons expressed as odds ratio (Fisher's exact test) relative to fetal neurons and glia. Repressor-promoter frequency in fetal and adult neurons expressed as odds ratio (Fisher's exact test) relative to glia. Numbers of enhancer-promoter and repressor-promoter loops for every dataset are shown. **(D)** Gene expression levels (counts per million reads mapped) associated with fetal and adult neuron differential enhancer-promoter loops across cell types. The significance of the gene expression differences between fetal cortical plate and adult neuronal samples associated with differential enhancer-promoter loops was determined using the Mann–Whitney test, and *P*-values are shown. **(E)** GO terms associated with differential enhancer-promoter and repressor-promoter loops across cell types. ·, nominally significant ($P < 0.05$); #, significant after FDR (Benjamini and Hochberg) correction (FDR < 0.05). **(F)** Violin plots showing fold difference in expression ($\log_{10}$(TPM)) of isoforms associated with exon-exon loops over isoforms not associated with loops. Wilcox test *P*-values shown above. **(G)** GO terms associated with exon-exon loops. ·, nominally significant ($P < 0.05$); #, significant after FDR (Benjamini and Hochberg) correction (FDR < 0.05).

whereas enhancer-promoter loops that are specific to the fetal cortical plate are associated with higher gene expression in the fetal cortical plate (Figure 4D, Supplementary Tables S14 and S15). The former are more strongly associated with pathways involved in synaptic structure and modulation of synaptic transmission, while the latter are more strongly associated with forebrain development, showing dynamic rewiring of enhancer-promoter loops to promote neuronal maturation (Figure 4E). Interestingly, among the genes associated with differential enhancer-promoter loops in adult neurons that show the highest fold increase in expression, we find *LINC00507* (Supplementary Table S15), a lncRNA that was previously found to be expressed exclusively in both human and non-human primate cortex in an age dependent manner, showing very basal expression in the gestational/infant group, but much higher expression in the adult group (74). We also identify genes involved in neuronal signaling, such as *RGS4*, a regulator of G protein signaling implicated in both BD and SCZ, and *HTRB*, a G-protein coupled serotonin receptor that causes fast, depolarizing responses in neurons after activation. Therefore, maturation of neurons is associated with an increased frequency of enhancer-promoter interactions that specifically up regulate neuronal activity related genes. Interestingly, repressor-promoter loops in both the fetal cortical plate and adult neurons, but not in glia, are strongly enriched for processes related to the positive regulation of transcription from an RNA pol II promoter.

Co-transcriptional splicing is widespread in the human brain (75), suggesting that isoform selection during gene expression occurs primarily on chromatin. A recent study on cohesin-mediated chromatin loops in different cell lines showed a cell type specific increase in the usage of exons that are proximal to gene body loop anchors linked to the promoter (76). Furthermore, another study found a role for CTCF in regulating alternative splicing by mediating intragenic looping (77). Altogether, these studies led us to hypothesize that intra-gene body chromatin loops may be associated with cell type specific isoform level transcription regulation in the human brain. To determine the gene loops, we used the gene-code annotation (GENCODEV30) and defined an isoform as a loop-isoform if both of the gene loop anchors overlapped with the exons within the isoform. To avoid potential bias from gene length, we normalized the isoform-level gene expression into TPM, and determined the median non-loop isoform and the median loop-isoform expression level. Thus, we quantified the relationship between the expression of isoforms containing specific exon pairs and the intragenic interaction frequency between those exons in our Hi-C data. Loop associated isoforms are more highly expressed in all cell types than non-loop isoforms (Figure 4F). As expected, exon-exon loops in fetal neurons are associated with early processes of differentiation, forebrain development, and regulation of axonogenesis (Figure 4G). These findings correlate gene looping with isoform usage and biological function during development.

Discussion

In this study, we sought to elucidate the functional relationships between the 3D genome, the epigenome and gene expression in the human brain. We focused on large scale differences in compartment and TAD structure between neurons and glia, as well as fine-scale changes in regulatory loops across neural development. Firstly, our initial discovery of higher contact densities <1 MB in neurons versus glia, which is followed by a steep decline in chromatin interaction frequencies at distances > 1 MB, allowed us to infer differences in genome compartmentalization. Indeed, we found that local compartmentalization patterns are disrupted in neurons, with a tendency to generate stronger TADs, which emerge during fetal development. These observations, along with the different patterns of A–A and B–B compartment interactions across genomic distance between neurons and glia, suggests a possible mechanism of loop extrusion in neuronal 3D genome organization. For example, the decrease in long range (>10 MB) B–B compartment interactions in neurons relative to glia is suggestive of loop extrusion as it correlates with findings from a recent study in which depletion of the STAG1 containing variant of cohesin, which is proposed to play a prominent role in TAD stabilization along with CTCF, was shown to increase long-range interactions between regions that were predominantly located in B compartments (78).

The lower frequency of CTCF footprints in OCRs in neurons compared to glia may also explain the decrease in compartmentalization. A recent study showed that depletion of CTCF alters local compartmental interactions, revealing a previously underappreciated role for CTCF in genome compartmentalization (79). The study showed that the loss of local compartmentalization after CTCF depletion specifically results in disruption of local A–A but not local B–B interactions, which are actually strengthened. The decrease in A–A compartment interactions relative to B–B interactions within 1–10 MB compared to the long range >10 MB compartment interactions in neurons versus glia correlates with these findings. In neurons, the less frequent binding of CTCF could allow extended loop extrusion which disrupts fine scale compartmentalization, thus producing similar results as the study cited above.

A recent study showed that cohesin release by WAPL in mouse neural progenitor cells is required to maintain a cohesin loading cycle to preserve lineage specific transcription (62). WAPL depletion leads to decreased interactions < 1 MB (defined as intra-TAD), but increased interactions within 1–10 MB (defined as inter-TAD). This observation suggests that a dynamic cohesin loading cycle is required to maintain interactions within TADs. Interestingly, we detect decreased inter-TAD (1–10 MB) versus intra-TAD A–A compartment interactions in fetal cortical plate and adult neurons relative to glia. This finding suggests that dynamic loading of cohesin throughout neural development may increase the probability of a subset of neural specific enhancers to interact with their target promoters within TADs, rather than forming aberrant interactions across TADs. Altogether, our results suggest that neurons show a higher order chromatin organization that is characterized by strong local folding of active chromatin, and the formation of strong A–A compartment interactions across large genomic regions that tend to be inactive.

We show that neurons and microglia, which have different developmental origins in the brain, have large scale differences in compartment structure, and these are correlated with their lineage specific functions. We also show that most neuronal A/B compartments are established during early human brain development and are preserved during adulthood. We find that the neuronal 3D genome is largely associated with B compartments enriched for polycomb repressed regions and non-active promoters. The biological implication of these findings

is that adult neuronal identity may be dependent on keeping a larger fraction of the genome suppressed in B compartments while activating a smaller fraction of the genome within A compartments. Previous studies have identified long-range polycomb-associated interactions in ES cells and human cell lines (11,80–86). However, to our knowledge, the role of polycomb associated long-range interactions in neurons has not been explored. We find that differential B compartments in adult neurons are enriched for genes that were shown to be implicated in neurodegeneration. These findings corroborate recent work in mice that showed the polycomb repressive complex, PRC2, to have a neuroprotective role (69). Our data also indicates that some of the genes that are upregulated in both PRC2 deficient mouse neurons and HD patients (including *POU4F1*, *POU4F2*, *HAND2*, *NKX2-5* and *TWIST1*) are in a non-active state, and form loops with distal polycomb repressed elements in adult neurons. Furthermore, *HAND2* and *NKX2-5* are involved in cardiac morphogenesis, suggesting that distal polycomb repressed elements contribute to neural specification and survival through suppression of non-neural developmental genes. It should be noted, however, that the differential expression in HD patients was measured in bulk tissue, and the perceived up-regulation of non-neural genes may be partially due to the neuronal loss characteristic of HD, rather than as a direct consequence of loss of polycomb repression in neurons.

Differential TAD boundaries in neurons show strong enrichment for active TSSs, which tend to be non-active in glia. Our results correlate with another study on the dynamic changes in the 3D genome during mouse neural differentiation *in vitro* that identified *de novo* TADs associated with mouse neural gene activation (11). We performed CRISPRi on *CNTNAP2*, and showed that local transcription inactivation is correlated with specific loss of insulation at the TSS proximal domain boundary. As cohesin was shown to be recruited to TSS and translocated in the direction of transcription (87), along with recent evidence demonstrating that transcription-dependent cohesin repositioning rewires chromatin loops (88), neuronal differential TADs may form primarily through loop extrusion that is influenced, at least partially, by transcriptional activity. A more recent study showed that RNA pol II could serve as a barrier to loop extrusion (89). Active genes were more strongly insulated than inactive genes, and contact enrichment and insulation corresponded to cohesin accumulation at TSSs. Insulation at these genes was abolished when knocking down the cohesin component SMC3, while CTCF KO or lack of proximal CTCF binding only partially weakens insulation. Interestingly, a recent study showed that inserting a construct containing a CTCF binding site and a TSS into the genome can generate a *de novo* domain around the insertion site (90). Importantly, at certain loci, removal of the CTCF binding site from the insertions spared transcription and did not disrupt the newly formed domain despite weakened insulation at the insertion locus, but removal of the TSS largely eliminated the *de novo* domain and reduced cohesin binding and chromatin folding at the TSS proximal region. Therefore, complementing other recent studies, transcription appears to play a role in loop extrusion in certain biological contexts.

Nonetheless, we cannot discard the alternative hypothesis that CTCF binding at differential TAD boundaries can influence transcription. We find an asymmetric H3K4me3 and H3K27ac enrichment within neuronal differential TADs relative to glia. A recent study showed that CTCF enriched loop anchors tend to show an asymmetric H3K4me3 and H3K27ac enrichment on the inside of the loop (91). Furthermore, another study showed that CTCF binds proximally to lineage specific promoters in mouse neural progenitor cells, promoting interactions with distal enhancers that are sparsely distributed within the local chromatin environment (92). They suggest that this may imply a predominantly asymmetric loop extrusion mechanism that reels distal enhancers towards the promoter. In fact, mouse homologues of some of the genes that we find proximal to differential TAD boundaries (including *CNTN5*, *CNTNAP2*, *CNTNAP5*, *FLRT2*, *FLRT3*, *GABRA1* and *GRIA4*) have been shown to be downregulated in cultured mouse cortical neurons upon knockdown of the cohesin component RAD21 (93). Interestingly, a recent study showed that E-P specificity can be determined by CTCF binding at the promoter, in a cohesin-dependent manner (94). Altogether, there may be a reciprocal relationship between transcription and 3D chromatin structure. Future work will need to explore the relationships between CTCF, cohesin and neural lineage specific transcription factors in cultured human neurons to elucidate the mechanisms behind the formation of neuronal differential TADs.

It should be noted that cohesin may only play an important role for the regulation of a small number of genes involved in neurodevelopmental processes, whereas activity dependent gene regulation may largely involve enhancer-promoter interactions that do not directly require cohesin (67). The genes that are found in the vicinity of neuronal differential TAD boundaries are involved in neurodevelopmental processes such as cell-to-cell adhesion and synapse organization. Conversely, in our study, the enhancer-promoter interactions that are gained in adult neurons versus fetal neurons are mainly involved in the modulation of synaptic activity, and the genes associated with these differential enhancer-promoter loops that show the strongest up regulation of expression are not located in the vicinity of differential TAD boundaries. Furthermore, the dependence of neuronal gene expression on cohesin was shown to scale with chromatin loop length, whereby the degree to which genes rely on cohesin scales with the genomic distance traversed by their chromatin contacts (67). The genes found in the proximity of differential TAD boundaries that we highlight in our study are associated with the formation of large loop domains. These domains may form during early development, but much of the dynamic change in the chromatin interactome from mid gestation to adulthood may involve enhancer-promoter interactions that are not directly reliant on the formation of TADs.

Interestingly, our data shows a larger increase in enhancer-promoter loops than repressor-promoter loops across neural development. A large proportion of repressor-promoter loops may already form during early development as part of the cell fate specification process, with only minor gains during neural maturation. Furthermore, we found that repressor-promoter loops in both fetal and adult neurons, but not in glia, are enriched for processes associated with the positive regulation of transcription from RNA pol II promoters. Given that neurons are highly specialized cell types, they may need to control factors implicated in the positive regulation of gene expression to prevent non-specific gene activation during neural development. Therefore, distal polycomb associated repressor elements may suppress the expression of genes involved in RNA pol II activation.

Altogether, our survey of the 3D genome during human brain development offers insights on the relationships between gene expression and chromatin organization from compartment level structure to loops. In particular, we show that cell type specific differences between neurons and glia involve broad scale reorganization of compartment/TAD structure, whereas during neural development to adulthood, changes in the 3D genome mainly involve fine-tuning of enhancer-promoter loops.

Data availability

The source data described in this manuscript are available via the PsychENCODE Knowledge Portal (https://psychencode.synapse.org/). The PsychENCODE Knowledge Portal is a platform for accessing data, analyses and tools generated through grants funded by the National Institute of Mental Health (NIMH) PsychENCODE program. Data is available for general research use according to the following requirements for data access and data attribution: (https://psychencode.synapse.org/DataAccess). For access to content described in this manuscript see: http://doi.org/10.7303/syn26164834. Raw data can be downloaded from http://doi.org/10.7303/syn26148119. Code used throughout this study is available at Zenodo (https://zenodo.org/record/8190413).

Supplementary data

Supplementary Data are available at NAR Online.

Acknowledgements

We thank the patients and families who donated material for these studies. We thank the computational resources and staff expertise provided by the Scientific Computing group at the Icahn School of Medicine at Mount Sinai.

Author contributions: **Samir Rahman**: Conceptualization, Methodology, Validation, Writing-original draft. **Pengfei Dong**: Conceptualization, Formal analysis, Methodology, Validation, Writing-review and editing. **Pasha Apontes**: Methodology, Writing-review and editing. **Michael B. Fernando**: Methodology, Validation. **Roman Kosoy**: Formal Analysis, Methodology, Validation. **Kayla G. Townsley**: Methodology, Validation. **Kiran Girdhar**: Methodology. **Jaroslav Bendl**: Methodology. **Zhiping Shao**: Methodology. **Ruth Misir**: Methodology. **Nadia Tsankova**: Resources. **Steven P. Kleopoulos**: Methodology. **Kristen J. Brennand**: Funding Acquisition, Resources, Writing-review and editing. **John F. Fullard**: Supervision, Methodology, Writing-review and editing. **Panos Roussos**: Supervision, Conceptualization, Funding Acquisition, Resources, Writing-review and editing.

Funding

National Institute on Aging, National Institutes of Health [U01-MH116442 to P.R., R01-MH109897 to P.R., K.J.B., R01-MH109677 to P.R., R01-MH110921 to P.R. R01MH106056 to K.J.B., U01DA047880 to K.J.B., R01DA048279 to K.J.B., 6R56MH101454 to K.J.B., R01MH121074 to K.J.B.]; J.B. is partially supported by a National Alliance for Research on Schizophrenia & Depression (NARSAD) Young Investigator Grant [27209] from the Brain and Behavior Research Foundation (BBRF); P.D. is partially supported by a NARSAD Young Investigator Grant [29683] from the Brain and Behavior Research Foundation (BBRF); K.G. is partially supported by an Alzheimer's Association Research Fellowship [AARF-21-722582]. Funding for open access charge: NIH funding, payment by PO—purchase order.

Conflict of interest statement

None declared.

References

1. Lupiáñez,D.G., Spielmann,M. and Mundlos,S. (2016) Breaking TADs: how alterations of chromatin domains result in disease. *Trends Genet.*, **32**, 225–237.
2. Dekker,J. and Mirny,L. (2016) The 3D genome as moderator of chromosomal communication. *Cell*, **164**, 1110–1121.
3. Dixon,J.R., Gorkin,D.U. and Ren,B. (2016) Chromatin domains: the unit of chromosome organization. *Mol. Cell*, **62**, 668–680.
4. Lieberman-aiden,E., Berkum,N.L.V., Williams,L., Imakaev,M., Ragoczy,T., Telling,A., Amit,I., Lajoie,B.R., Sabo,P.J., Dorschner,M.O., *et al.* (2009) Comprehensive mapping of long-range interactions reveals folding principles of the Human genome. *Science*, **33292**, 289–293.
5. Dixon,J.R., Selvaraj,S., Yue,F., Kim,A., Li,Y., Shen,Y., Hu,M., Liu,J.S. and Ren,B. (2012) Topological domains in mammalian genomes identified by analysis of chromatin interactions. *Nature*, **485**, 376–380.
6. Nora,E.P., Lajoie,B.R., Schulz,E.G., Giorgetti,L., Okamoto,I., Servant,N., Piolot,T., Van Berkum,N.L., Meisig,J., Sedat,J., *et al.* (2012) Spatial partitioning of the regulatory landscape of the X-inactivation centre. *Nature*, **485**, 381–385.
7. Lupiáñez,D.G., Kraft,K., Heinrich,V., Krawitz,P., Brancati,F., Klopocki,E., Horn,D., Kayserili,H., Opitz,J.M., Laxova,R., *et al.* (2015) Disruptions of topological chromatin domains cause pathogenic rewiring of gene-enhancer interactions. *Cell*, **161**, 1012–1025.
8. Kishi,Y. and Gotoh,Y. (2018) Regulation of chromatin structure during neural development. *Front. Neurosci.*, **12**, 874.
9. Fraser,J., Ferrai,C., Chiariello,A.M., Schueler,M., Rito,T., Laudanno,G., Barbieri,M., Moore,B.L., Kraemer,D.C., Aitken,S., *et al.* (2015) Hierarchical folding and reorganization of chromosomes are linked to transcriptional changes in cellular differentiation. *Mol. Syst. Biol.*, **11**, 852.
10. Dixon,J.R., Jung,I., Selvaraj,S., Shen,Y., Antosiewicz-Bourget,J.E., Lee,A.Y., Ye,Z., Kim,A., Rajagopal,N., Xie,W., *et al.* (2015) Chromatin architecture reorganization during stem cell differentiation. *Nature*, **518**, 331–336.
11. Bonev,B., Mendelson Cohen,N., Szabo,Q., Fritsch,L., Papadopoulos,G.L., Lubling,Y., Xu,X., Lv,X., Hugnot,J.P., Tanay,A., *et al.* (2017) Multiscale 3D genome rewiring during mouse neural development. *Cell*, **171**, 557–572.
12. Won,H., De La Torre-Ubieta,L., Stein,J.L., Parikshak,N.N., Huang,J., Opland,C.K., Gandal,M.J., Sutton,G.J., Hormozdiari,F., Lu,D., *et al.* (2016) Chromosome conformation elucidates regulatory relationships in developing human brain. *Nature*, **538**, 523–527.
13. Rajararan,P., Borrman,T., Liao,W., Schrode,N., Flaherty,E., Casiño,C., Powell,S., Yashaswini,C., LaMarca,E., Kassim,B., *et al.* (2018) Neuron-specific signatures in the chromosomal connectome are associated with Schizophrenia risk. *Science*, **362**, eaat4311.
14. Roussos,P., Mitchell,A.C., Voloudakis,G., Fullard,J.F., Pothula,V.M., Tsang,J., Stahl,E.A., Georgakopoulos,A., Ruderfer,D.M., Charney,A., *et al.* (2014) A role for noncoding variation in schizophrenia. *Cell Rep.*, **9**, 1417–1429.
15. Hu,B., Won,H., Mah,W., Park,R.B., Kassim,B., Spiess,K., Kozlenkov,A., Crowley,C.A., Pochareddy,S., Ashley-Koch,A.E.,

et al. (2021) Neuronal and glial 3D chromatin architecture informs the cellular etiology of brain disorders. *Nat. Commun.*, **12**, 3968.
16. Song,M., Pebworth,M.P., Yang,X., Abnousi,A., Fan,C., Wen,J., Rosen,J.D., Choudhary,M.N.K., Cui,X., Jones,I.R., *et al.* (2020) Cell-type-specific 3D epigenomes in the developing human cortex. *Nature*, **587**, 644–649.
17. Nott,A., Holtman,I.R., Coufal,N.G., Schlachetzki,J.C.M., Yu,M., Hu,R., Han,C.Z., Pena,M., Xiao,J., Wu,Y., *et al.* (2019) Brain cell type-specific enhancer-promoter interactome maps and disease risk association. *Science*, **366**, 1134–1139.
18. Rao,S.S.P., Huntley,M.H., Durand,N.C., Stamenova,E.K., Bochkov,I.D., Robinson,J.T., Sanborn,A.L., Machol,I., Omer,A.D., Lander,E.S., *et al.* (2014) A 3D map of the human genome at kilobase resolution reveals principles of chromatin looping. *Cell*, **159**, 1665–1680.
19. Brind'Amour,J., Liu,S., Hudson,M., Chen,C., Karimi,M.M. and Lorincz,M.C. (2015) An ultra-low-input native ChIP-seq protocol for genome-wide profiling of rare cell populations. *Nat. Commun.*, **6**, 6033.
20. Dobin,A., Davis,C.A., Schlesinger,F., Drenkow,J., Zaleski,C., Jha,S., Batut,P., Chaisson,M. and Gingeras,T.R. (2013) STAR: ultrafast universal RNA-seq aligner. *Bioinformatics*, **29**, 15–21.
21. Van De Geijn,B., Mcvicker,G., Gilad,Y. and Pritchard,J.K. (2015) WASP: allele-specific software for robust molecular quantitative trait locus discovery. *Nat. Methods*, **12**, 1061–1063.
22. Li,B. and Dewey,C.N. (2011) RSEM: accurate transcript quantification from RNA-seq data with or without a reference genome. *BMC Bioinf.*, **12**, 323.
23. Deluca,D.S., Levin,J.Z., Sivachenko,A., Fennell,T., Nazaire,M.D., Williams,C., Reich,M., Winckler,W. and Getz,G. (2012) RNA-SeQC: rNA-seq metrics for quality control and process optimization. *Bioinformatics*, **28**, 1530–1532.
24. Fromer,M., Roussos,P., Sieberts,S.K., Johnson,J.S., Kavanagh,D.H., Perumal,T.M., Ruderfer,D.M., Oh,E.C., Topol,A., Shah,H.R., *et al.* (2016) Gene expression elucidates functional impact of polygenic risk for schizophrenia. *Nat. Neurosci.*, **19**, 1442–1453.
25. Lake,B.B., Chen,S., Sos,B.C., Fan,J., Kaeser,G.E., Yung,Y.C., Duong,T.E., Gao,D., Chun,J., Kharchenko,P.V., *et al.* (2018) Integrative single-cell analysis of transcriptional and epigenetic states in the human adult brain. *Nat. Biotechnol.*, **36**, 70–80.
26. Zhu,K., Bendl,J., Rahman,S., Vicari,J.M., Coleman,C., Clarence,T., Latouche,O., Tsankova,N.M., Li,A., Brennand,K.J., *et al.* (2022) Multi-omic profiling of the developing human cerebral cortex at the single cell level. bioRxiv doi: https://doi.org/10.1101/2022.10.14.512250, 17 October 2022, preprint: not peer reviewed.
27. Hunt,G.J., Freytag,S., Bahlo,M. and Gagnon-Bartsch,J.A. (2019) Dtangle: accurate and robust cell type deconvolution. *Bioinformatics*, **35**, 2093–2099.
28. Ernst,J. and Kellis,M. (2012) ChromHMM: automating chromatin-state discovery and characterization. *Nat. Methods*, **9**, 215–216.
29. Servant,N., Varoquaux,N., Lajoie,B.R., Viara,E., Chen,C.J., Vert,J.P., Heard,E., Dekker,J. and Barillot,E. (2015) HiC-Pro: an optimized and flexible pipeline for Hi-C data processing. *Genome Biol.*, **16**, 259.
30. Langmead,B. and Salzberg,S.L. (2012) Fast gapped-read alignment with Bowtie 2. *Nat. Methods*, **9**, 357–359.
31. Imakaev,M., Fudenberg,G., McCord,R.P., Naumova,N., Goloborodko,A., Lajoie,B.R., Dekker,J. and Mirny,L.A. (2012) Iterative correction of hi-C data reveals hallmarks of chromosome organization. *Nat. Methods*, **9**, 999–1003.
32. Yang,T., Zhang,F., Yardımci,G.G., Song,F., Hardison,R.C., Noble,W.S., Yue,F. and Li,Q. (2017) HiCRep: assessing the reproducibility of hi-C data using a stratum-adjusted correlation coefficient. *Genome Res.*, **27**, 1939–1949.
33. Zheng,X. and Zheng,Y. (2018) CscoreTool: fast hi-C compartment analysis at high resolution. *Bioinformatics*, **34**, 1568–1570.
34. Liberzon,A., Subramanian,A., Pinchback,R., Thorvaldsdóttir,H., Tamayo,P. and Mesirov,J.P. (2011) Molecular signatures database (MSigDB) 3.0. *Bioinformatics*, **27**, 1739–1740.
35. Labadorf,A., Hoss,A.G., Lagomarsino,V., Latourelle,J.C., Hadzi,T.C., Bregu,J., MacDonald,M.E., Gusella,J.F., Chen,J.F., Akbarian,S., *et al.* (2015) RNA sequence analysis of human huntington disease brain reveals an extensive increase in inflammatory and developmental gene expression. *PLoS One*, **10**, e0143563.
36. Shin,H., Shi,Y., Dai,C., Tjong,H., Gong,K., Alber,F. and Zhou,X.J. (2015) TopDom: an efficient and deterministic method for identifying topological domains in genomes. *Nucleic Acids Res.*, **44**, e70.
37. Crane,E., Bian,Q., McCord,R.P., Lajoie,B.R., Wheeler,B.S., Ralston,E.J., Uzawa,S., Dekker,J. and Meyer,B.J. (2015) Condensin-driven remodelling of X chromosome topology during dosage compensation. *Nature*, **523**, 240–244.
38. Robinson,M.D. and Oshlack,A. (2010) A scaling normalization method for differential expression analysis of RNA-seq data. *Genome Biol.*, **11**, R25.
39. Liu,R., Holik,A.Z., Su,S., Jansz,N., Chen,K., Leong,H.S., Blewitt,M.E., Asselin-Labat,M.L., Smyth,G.K. and Ritchie,M.E. (2015) Why weight? Modelling sample and observational level variability improves power in RNA-seq analyses. *Nucleic Acids Res.*, **43**, e97.
40. Hoffman,G.E. and Roussos,P. (2021) Dream: powerful differential expression analysis for repeated measures designs. *Bioinformatics*, **37**, 192–201.
41. Hoffman,G.E. and Schadt,E.E. (2016) variancePartition: interpreting drivers of variation in complex gene expression studies. *BMC Bioinf.*, **17**, 17–22.
42. Durand,N.C., Shamim,M.S., Machol,I., Rao,S.S.P., Huntley,M.H., Lander,E.S. and Aiden,E.L. (2016) Juicer provides a one-click system for analyzing loop-resolution hi-C experiments. *Cell Syst.*, **3**, 95–98.
43. Ay,F., Bailey,T.L. and Noble,W.S. (2014) Statistical confidence estimation for hi-C data reveals regulatory chromatin contacts. *Genome Res.*, **24**, 999–1011.
44. Finucane,H.K., Bulik-Sullivan,B., Gusev,A., Trynka,G., Reshef,Y., Loh,P.R., Anttila,V., Xu,H., Zang,C., Farh,K., *et al.* (2015) Partitioning heritability by functional annotation using genome-wide association summary statistics. *Nat. Genet.*, **47**, 1228–1235.
45. Stahl,E.A., Breen,G., Forstner,A.J., McQuillin,A., Ripke,S., Trubetskoy,V., Mattheisen,M., Wang,Y., Coleman,J.R.I., Gaspar,H.A., *et al.* (2019) Genome-wide association study identifies 30 loci associated with bipolar disorder. *Nat. Genet.*, **51**, 793–803.
46. Trubetskoy,V., Pardinas,A.F., Qi,T., Panagiotaropoulou,G., Awasthi,S., Bigdeli,T.B., Bryois,J., Chen,C.-Y., Dennison,C.A., Hall,L.S., *et al.* (2022) Mapping genomic loci implicates genes and synaptic biology in schizophrenia. *Nature*, **604**, 502–508.
47. Ruderfer,D.M., Ripke,S., McQuillin,A., Boocock,J., Stahl,E.A., Pavlides,J.M.W., Mullins,N., Charney,A.W., Ori,A.P.S., Loohuis,L.M.O., *et al.* (2018) Genomic dissection of bipolar disorder and schizophrenia, including 28 subphenotypes. *Cell*, **173**, 1705–1715.
48. Demontis,D., Walters,R.K., Martin,J., Mattheisen,M., Als,T.D., Agerbo,E., Baldursson,G., Belliveau,R., Bybjerg-Grauholm,J., Bækvad-Hansen,M., *et al.* (2019) Discovery of the first genome-wide significant risk loci for attention deficit/hyperactivity disorder. *Nat. Genet.*, **51**, 63–75.
49. Karlsson Linnér,R., Biroli,P., Kong,E., Meddens,S.F.W., Wedow,R., Fontana,M.A., Lebreton,M., Tino,S.P., Abdellaoui,A., Hammerschlag,A.R., *et al.* (2019) Genome-wide association analyses of risk tolerance and risky behaviors in over 1 million individuals identify hundreds of loci and shared genetic influences. *Nat. Genet.*, **51**, 245–257.

50. Nagel,M., Watanabe,K., Stringer,S., Posthuma,D. and Van Der Sluis,S. (2018) Item-level analyses reveal genetic heterogeneity in neuroticism. *Nat. Commun.*, **9**, 905.
51. Jansen,P.R., Watanabe,K., Stringer,S., Skene,N., Bryois,J., Hammerschlag,A.R., de Leeuw,C.A., Benjamins,J.S., Muñoz-Manchado,A.B., Nagel,M., *et al.* (2019) Genome-wide analysis of insomnia in 1,331,010 individuals identifies new risk loci and functional pathways. *Nat. Genet.*, **51**, 394–403.
52. International HapMap Consortium (2003) International HapMap Consortium. The International HapMap Project. *Nature*, **426**, 789–796.
53. Auton,A., Abecasis,G.R., Altshuler,D.M., Durbin,R.M., Bentley,D.R., Chakravarti,A., Clark,A.G., Donnelly,P., Eichler,E.E., Flicek,P., *et al.* (2015) A global reference for human genetic variation. *Nature*, **526**, 68–74.
54. Bystron,I., Blakemore,C. and Rakic,P. (2008) Development of the human cerebral cortex: boulder Committee revisited. *Nat. Rev. Neurosci.*, **9**, 110–122.
55. Rakic,P. (1972) Mode of cell migration to the superficial layers of fetal monkey neocortex. *J. Comp. Neurol.*, **145**, 61–83.
56. Rakic,P. (2003) Developmental and evolutionary adaptations of cortical radial glia. *Cereb. Cortex*, **13**, 541–549.
57. Kwan,K.Y., Šestan,N. and Anton,E.S. (2012) Transcriptional co-regulation of neuronal migration and laminar identity in the neocortex. *Development*, **139**, 1535–1546.
58. Kosoy,R., Fullard,J.F., Zeng,B., Bendl,J., Dong,P., Rahman,S., Kleopoulos,S.P., Shao,Z., Girdhar,K., Humphrey,J., *et al.* (2022) Genetics of the human microglia regulome refines Alzheimer's disease risk loci. *Nat. Genet.*, **54**, 1145–1154.
59. de la Torre-Ubieta,L., Stein,J.L., Won,H., Opland,C.K., Liang,D., Lu,D. and Geschwind,D.H. (2018) The dynamic landscape of open chromatin during Human cortical neurogenesis. *Cell*, **172**, 289–304.
60. Nuebler,J., Fudenberg,G., Imakaev,M., Abdennur,N. and Mirny,L.A. (2018) Chromatin organization by an interplay of loop extrusion and compartmental segregation. *Proc. Natl. Acad. Sci. U.S.A.*, **115**, E6697–E6706.
61. Schwarzer,W., Abdennur,N., Goloborodko,A., Pekowska,A., Fudenberg,G., Loe-Mie,Y., Fonseca,N.A., Huber,W., Haering,C.H., Mirny,L., *et al.* (2017) Two independent modes of chromatin organization revealed by cohesin removal. *Nature*, **551**, 51–56.
62. Liu,N.Q., Maresca,M., Brand,T.V.D., Braccioli,L., Schijns,M.M.G.A., Teunissen,H., Bruneau,B.G., Nora,P. and Wit,E.D. (2020) WAPL maintains a cohesin loading cycle to preserve cell-type-specific distal gene regulation. *Nat. Genet.*, **53**, 100–109.
63. Weirauch,M.T., Yang,A., Albu,M., Cote,A.G., Montenegro-Montero,A., Drewe,P., Najafabadi,H.S., Lambert,S.A., Mann,I., Cook,K., *et al.* (2014) Determination and inference of eukaryotic transcription factor sequence specificity. *Cell*, **158**, 1431–1443.
64. Bentsen,M., Goymann,P., Schultheis,H., Klee,K., Petrova,A., Wiegandt,R., Fust,A., Preussner,J., Kuenne,C., Braun,T., *et al.* (2020) ATAC-seq footprinting unravels kinetics of transcription factor binding during zygotic genome activation. *Nat. Commun.*, **11**, 4267.
65. Buenrostro,J.D., Giresi,P.G., Zaba,L.C., Chang,H.Y. and Greenleaf,W.J. (2013) Transposition of native chromatin for fast and sensitive epigenomic profiling of open chromatin, DNA-binding proteins and nucleosome position. *Nat. Methods*, **10**, 1213–1218.
66. Sun,Y., Xu,X., Zhao,W., Zhang,Y., Chen,K., Li,Y., Wang,X., Zhang,M., Xue,B., Yu,W., *et al.* (2023) RAD21 is the core subunit of the cohesin complex involved in directing genome organization. *Genome Biol.*, **24**, 155.
67. Calderon,L., Weiss,F.D., Beagan,J.A., Oliveira,M.S., Georgieva,R., Wang,Y.F., Carroll,T., Dharmalingam,G., Gong,W., Tossell,K., *et al.* (2022) Cohesin-dependence of neuronal gene expression relates to chromatin loop length. *eLife*, **11**, e76539.
68. Liu,P.P., Xu,Y.J., Teng,Z.Q. and Liu,C.M. (2018) Polycomb Repressive Complex 2: emerging roles in the Central nervous system. *Neuroscientist*, **24**, 208–220.
69. Von Schimmelmann,M., Feinberg,P.A., Sullivan,J.M., Ku,S.M., Badimon,A., Duff,M.K., Wang,Z., Lachmann,A., Dewell,S., Ma'ayan,A., *et al.* (2016) Polycomb repressive complex 2 (PRC2) silences genes responsible for neurodegeneration. *Nat. Neurosci.*, **19**, 1321–1330.
70. Zhao,L., Li,J., Ma,Y., Wang,J., Pan,W., Gao,K., Zhang,Z., Lu,T., Ruan,Y., Yue,W., *et al.* (2015) Ezh2 is involved in radial neuronal migration through regulating Reelin expression in cerebral cortex. *Sci. Rep.*, **5**, 15484.
71. Hoss,A.G., Kartha,V.K., Dong,X., Latourelle,J.C., Dumitriu,A., Hadzi,T.C., MacDonald,M.E., Gusella,J.F., Akbarian,S., Chen,J.F., *et al.* (2014) MicroRNAs located in the hox gene clusters are implicated in Huntington's Disease pathogenesis. *PLoS Genet.*, **10**, e1004188.
72. Dong,X., Tsuji,J., Labadorf,A., Roussos,P., Chen,J.F., Myers,R.H., Akbarian,S. and Weng,Z. (2015) The role of H3K4me3 in transcriptional regulation is altered in Huntington's disease. *PLoS One*, **10**, e0144398.
73. Schneider,M.F., Müller,V., Müller,S.A., Lichtenthaler,S.F., Becker,P.B. and Scheuermann,J.C. (2022) LncRNA RUS shapes the gene expression program towards neurogenesis. *Life Sci. Alliance*, **5**, e202201504.
74. Mills,J.D., Ward,M., Chen,B.J., Iyer,A.M., Aronica,E. and Janitz,M. (2016) LINC00507 Is specifically expressed in the primate cortex and has age-dependent expression patterns. *J. Mol. Neurosci.*, **59**, 431–439.
75. Ameur,A., Zaghlool,A., Halvardson,J., Wetterbom,A., Gyllensten,U., Cavelier,L. and Feuk,L. (2011) Total RNA sequencing reveals nascent transcription and widespread co-transcriptional splicing in the human brain. *Nat. Struct. Mol. Biol.*, **18**, 1435–1440.
76. Grubert,F., Srivas,R., Spacek,D.V., Kasowski,M., Ruiz-Velasco,M., Sinnott-Armstrong,N., Greenside,P., Narasimha,A., Liu,Q., Geller,B., *et al.* (2020) Landscape of cohesin-mediated chromatin loops in the human genome. *Nature*, **583**, 737–743.
77. Ruiz-Velasco,M., Kumar,M., Lai,M.C., Bhat,P., Solis-Pinson,A.B., Reyes,A., Kleinsorg,S., Noh,K.M., Gibson,T.J. and Zaugg,J.B. (2017) CTCF-mediated chromatin loops between promoter and gene body regulate alternative splicing across individuals. *Cell Syst.*, **5**, 628–637.
78. Kojic,A., Cuadrado,A., De Koninck,M., Giménez-Llorente,D., Rodríguez-Corsino,M., Gómez-López,G., Le Dily,F., Marti-Renom,M.A. and Losada,A. (2018) Distinct roles of cohesin-SA1 and cohesin-SA2 in 3D chromosome organization. *Nat. Struct. Mol. Biol.*, **25**, 496–504.
79. Zhang,H., Lam,J., Zhang,D., Lan,Y., Vermunt,M.W., Keller,C.A., Giardine,B., Hardison,R.C. and Blobel,G.A. (2021) CTCF and transcription influence chromatin structure re-configuration after mitosis. *Nat. Commun.*, **12**, 5157.
80. Du,Z. and Zheng,H. (2020) Polycomb group proteins regulate chromatin architecture in mouse oocytes and early embryos. *Mol. Cell*, **77**, 825–839.
81. Boyle,S., Flyamer,I.M., Williamson,I., Sengupta,D., Bickmore,W.A. and Illingworh,R.S. (2020) A central role for canonical PRC1 in shaping the 3D nuclear landscape. *Genes Dev.* , **34**, 931–949.
82. Rhodes,J.D.P., Feldmann,A., Hernández-Rodríguez,B., Díaz,N., Brown,J.M., Fursova,N.A., Blackledge,N.P., Prathapan,P., Dobrinic,P., Huseyin,M.K., *et al.* (2020) Cohesin disrupts polycomb-dependent chromosome interactions in embryonic stem cells. *Cell Rep.*, **30**, 820–835.
83. Zhang,X., Jeong,M., Huang,X., Wang,X.Q., Wang,X., Zhou,W., Shamim,M.S., Gore,H., Himadewi,P., Liu,Y., *et al.* (2020) Large DNA methylation nadirs anchor chromatin loops maintaining hematopoietic stem cell identity. *Mol. Cell*, **78**, 506–521.
84. Kraft,K., Yost,K.E., Murphy,S., Magg,A., Long,Y., Corces,M.R., Granja,J.M., Mundlos,S., Cech,T.R., Boettiger,A., *et al.* (2022)

Polycomb-mediated genome architecture enables long-range spreading of H3K27 methylation. *PNAS* ,**119**, e2201883119.
85. Cai,Y., Zhang,Y., Loh,Y.P., Tng,J.Q., Lim,M.C., Cao,Z., Raju,A., Lieberman Aiden,E., Li,S., Manikandan,L., *et al.* (2021) H3K27me3-rich genomic regions can function as silencers to repress gene expression via chromatin interactions. *Nat. Commun.*, **12**, 719.
86. Schoenfelder,S., Sugar,R., Dimond,A., Javierre,B.M., Armstrong,H., Mifsud,B., Dimitrova,E., Matheson,L., Tavares-Cadete,F., Furlan-Magaril,M., *et al.* (2015) Polycomb repressive complex PRC1 spatially constrains the mouse embryonic stem cell genome. *Nat. Genet.*, **47**, 1179–1186.
87. Busslinger,G.A., Stocsits,R.R., Van Der Lelij,P., Axelsson,E., Tedeschi,A., Galjart,N. and Peters,J.M. (2017) Cohesin is positioned in mammalian genomes by transcription, CTCF and wapl. *Nature*, **544**, 503–507.
88. Olan,I., Parry,A.J., Schoenfelder,S., Narita,M., Ito,Y., Chan,A.S.L., Slater,G.S.C., Bihary,D., Bando,M., Shirahige,K., *et al.* (2020) Transcription-dependent cohesin repositioning rewires chromatin loops in cellular senescence. *Nat. Commun.*, **11**, 6049.
89. Banigan,E.J., Tang,W., van den Berg,A.A., Stocsits,R.R, Wutz,G., Brandão,H.B., Busslinger,G.A., Peters,J.-M. and Mirny,L.A. (2023) Transcription shapes 3D chromatin organization by interacting with loop extrusion. *PNAS*, **120**, e2210480120.
90. Zhang,D., Huang,P., Sharma,M., Keller,C.A., Giardine,B., Zhang,H., Gilgenast,T.G., Phillips-Cremins,J.E., Hardison,R.C. and Blobel,G.A. (2020) Alteration of genome folding via contact domain boundary insertion. *Nat. Genet.*, **52**, 1076–1087.
91. Akgol Oksuz,B., Yang,L., Abraham,S., Venev,S.V, Krietenstein,N., Parsi,K.M., Ozadam,H., Oomen,M.E., Nand,A., Mao,H., *et al.* (2021) Systematic evaluation of chromosome conformation capture assays. *Nat. Methods*, **18**, 1046–1055.
92. Kubo,N., Ishii,H., Xiong,X., Bianco,S., Meitinger,F., Hu,R., Hocker,J.D., Conte,M., Gorkin,D., Yu,M., *et al.* (2021) Promoter-proximal CTCF binding promotes distal enhancer-dependent gene activation. *Nat. Struct. Mol. Biol.*, 28, 152–161.
93. Calderon,L., Weiss,F.D., Beagan,J.A., Oliveira,M.S., Wang,Y.-F., Carroll,T., Dharmalingam,G., Gong,W., Tossell,K., De Paola,V., *et al.* (2021) Activity-induced gene expression and long-range enhancer-promoter contacts in cohesin-deficient neurons. bioRxiv doi: https://doi.org/10.1101/2021.02.24.432639, 24 February 2021, preprint: not peer reviewed.
94. Oh,S., Shao,J., Mitra,J., Xiong,F., D'Antonio,M., Wang,R., Garcia-Bassets,I., Ma,Q., Zhu,X., Lee,J.-H., *et al.* (2021) Enhancer release and retargeting activates disease-susceptibility genes. *Nature*, 595, 735–740.

Received: March 3, 2023. **Revised:** August 18, 2023. **Editorial Decision:** September 17, 2023. **Accepted:** September 19, 2023